PREPRINT

Unraveling the mechanisms behind the triple isotopic composition of dissolved oxygen

Emeline Clermont[1,2], Ji-Woong Yang[1,2], Thomas Extier[3] and Didier M. Roche[1,2,4]

[1] Laboratoire des Sciences du Climat et de l'Environnement (LSCE), CEA, CNRS, UVSQ, Université Paris-Saclay, Gif-sur-Yvette, France
[2] Institut Pierre-Simon Laplace (IPSL), Université Versailles Saint-Quentin, Guyancourt, France
[3] Univ. Bordeaux, CNRS, Bordeaux INP, EPOC, UMR 5805, 33600 Pessac, France
[4] Earth and Climate Cluster, Faculty of Science, Vrije Universiteit Amsterdam, De Boelelaan 1085, 1081 HV Amsterdam, the Netherlands

Corresponding author

Emeline Clermont
Email: emeline.clermont@lsce.ispl.fr

Status

Submitted to Journal of Geophysical Research: Oceans.
This manuscript is a preprint and has not yet been peer reviewed.

Keywords

- Oxygen isotopes;
- Ocean;
- iLOVECLIM

Unraveling the mechanisms behind the triple isotopic composition of dissolved oxygen

Emeline Clermont[1,2], Ji-Woong Yang[1,2], Thomas Extier[3]and Didier M. Roche[1,2,4]

[1]Laboratoire des Sciences du Climat et de l'Environnement (LSCE), CEA, CNRS, UVSQ, Université Paris-Saclay, Gif-sur-Yvette, France
[2]Institut Pierre-Simon Laplace (IPSL), Université Versailles Saint-Quentin, Guyancourt, France
[3]Univ. Bordeaux, CNRS, Bordeaux INP, EPOC, UMR 5805, 33600 Pessac, France
[4]Earth and Climate Cluster, Faculty of Science, Vrije Universiteit Amsterdam, De Boelelaan 1085, 1081 HV Amsterdam, the Netherlands

Key Points:

- Photosynthesis dominates the ocean triple oxygen isotope signal, confirming its first-order sensitivity to biological oxygen production.
- Sensitivity experiments constrain the 17O/18O isotope fractionation during respiration to 0.517, a key parameter for representing this proxy.
- The model captures large-scale patterns but not local variability, pointing to unresolved subgrid-scale processes and observational gaps.

Corresponding author: Emeline Clermont, emeline.clermont@lsce.ipsl.fr

Abstract

Estimating the evolution of biospheric oxygen production through time is a major challenge. The triple oxygen isotope composition of molecular oxygen ($^{17}\Delta$) has been proposed as a tracer of this production, as it integrates contributions from marine ($^{17}\Delta_{\text{ocean}}$) and terrestrial ($^{17}\Delta_{\text{terr}}$) biospheric oxygen. The recent implementation of $^{17}\Delta_{\text{ocean}}$ in the intermediate-complexity climate model iLOVECLIM now enables a mechanistic exploration of this proxy. This study aims to improve our understanding of the behavior and limitations of $^{17}\Delta_{\text{ocean}}$ as an indicator of biological oxygen production across spatial scales. At large scales, the $^{17}\Delta_{\text{ocean}}$ signal primarily reflects residual processes affecting dissolved oxygen, with photosynthesis exerting dominant control on its magnitude and variability. Our results further highlight the strong sensitivity of the simulated signal to biological isotopic fractionations. Sensitivity experiments based on a Latin hypercube approach constrain the $^{17}O/^{18}O$ fractionation during respiration to 0.517. While the model captures large-scale patterns and overall variability of $\delta^{18}O$–O_2 and $^{17}\Delta_{\text{ocean}}$, it cannot reproduce their local variability. This mismatch reflects subgrid-scale variability that the model cannot resolve, as it represents grid-cell averages rather than individual observations. Consequently, no combination of biological fractionation coefficient fully reproduces the observed $^{17}\Delta_{\text{ocean}}$ signal, pointing to both model limitations and observational uncertainties. Overall, these results confirm the first-order sensitivity of $^{17}\Delta_{\text{ocean}}$ to photosynthetic processes, while indicating that its finer interpretation in global models remains uncertain. This calls for a reassessment of the isotopic and biological processes governing this proxy, and for improved observational constraints.

Plain Language Summary

Understanding how much oxygen living organisms produce, and how this has changed through time, is a major scientific challenge. One promising approach relies on measuring the triple isotopic composition of dissolved oxygen in the ocean, called $^{17}\Delta_{\text{ocean}}$, which carries a subtle fingerprint of photosynthesis and has the potential to provide insights on oceanic biological oxygen production. In this study, we used a numerical climate model to simulate this oxygen isotope signal across the ocean and investigate the processes that control it. Our results confirm that photosynthesis is the dominant driver of the signal at large scales. However, we also show that the signal is highly sensitive to how organisms fractionate oxygen isotopes during respiration, a process that remains poorly constrained. While the model reproduces broad oceanic patterns, it fails to capture the local variability observed in the data, reflecting the limits of models that average processes over large grid cells. These findings indicate that interpreting this isotopic tracer in global models is more uncertain than previously assumed. Improving our understanding of biological isotope effects, together with more spatially resolved observations, will be essential to fully exploit the potential of this proxy for reconstructing oxygen production.

1 Introduction

The ocean is a major sink for atmospheric CO_2 and a key regulator of climate (Friedlingstein et al., 2025). Marine primary productivity drives carbon fixation and oxygen production, making it a central component of the global carbon cycle. Yet, quantifying marine biological oxygen production and the associated carbon fluxes remains a major challenge. The triple oxygen isotope composition of dissolved oxygen ($^{17}\Delta_{\text{ocean}}$) has been proposed as a promising tracer of marine productivity (Luz & Barkan, 2000). The $^{17}\Delta_{\text{ocean}}$ signal reflects a balance between biological and physical processes: photosynthesis and respiration induce isotope fractionation, while air-sea gas exchange and ocean circulation redistribute and dilute these signatures. As a result, the value of $^{17}\Delta_{\text{ocean}}$ depends on both biological O_2 production and gas exchange with the atmosphere. The gas exchange rate tends to bring the value of $^{17}\Delta_{\text{ocean}}$ into equilibrium with the air. Conversely, the

rate of biological production tends to raise the $^{17}\Delta_{\text{ocean}}$ concentration to a maximum value (Luz & Barkan, 2000). Thus, $^{17}\Delta_{\text{ocean}}$ is expected to vary between these two end-members, that is between 0 and 249 ppm.

At the global scale, the triple isotopic composition of atmospheric oxygen ($^{17}\Delta$) is a proxy of gross photosynthetic O_2 flux. Measured in ice cores, $^{17}\Delta$ integrates contributions from the marine biosphere, the terrestrial biosphere, and the stratosphere. In the stratosphere, the $^{17}O/^{16}O$ and $^{18}O/^{16}O$ ratios are affected by photochemical reactions between O_2, CO_2, and O_3, leading to mass-independent oxygen fractionation (Thiemens et al., 1991; M. Bender et al., 1994; Luz et al., 1999). Conversely, biological processes associated with the terrestrial and marine biosphere generate mass-dependent fractionation, such that the $^{17}O/^{16}O$ ratio is approximately half that of $^{18}O/^{16}O$ (Luz et al., 1999; Luz & Barkan, 2000, 2005). Thus, $^{17}\Delta$ represents the ^{17}O anomaly and is defined by the following equation (Miller, 2002):

$$^{17}\Delta = \left[\ln\left(1+\frac{\delta^{17}O}{1000}\right) - \lambda \times \ln\left(1+\frac{\delta^{18}O}{1000}\right)\right] \times 1\,000\,000 \quad (1)$$

Where: δ^*O is derived from the isotopic ratio of the sample (R*) relative to the isotopic reference standard (R_{std}): $\delta^*O = ({}^*R \,/\, {}^*R_{std}\text{ -1}) \times 1000$, where * denotes either 17 or 18. The isotopic ratio R* corresponds to the abundance ratio between the heavy isotopologues ($^{17}O^{16}O$) and $^{18}O^{16}O$) and the most common isotopologue ($^{16}O^{16}O$). Air O_2 is used as the isotopic standard (Luz & Barkan, 2005). The $\delta^{17}O$–O_2 anomaly is defined relative to the mass-dependent fractionation line with a characteristic triple-isotope slope $\lambda = 0.518$, which reflects biological fractionation processes (Luz & Barkan, 2005). Because the $^{17}\Delta$ variations are extremely small, they are expressed in ppm (1 ppm = 0.001 ‰) relative to air.

However, the behavior of $^{17}\Delta_{\text{ocean}}$ remains uncertain (Li et al., 2022). Physical processes can influence its distribution, while biological fractionation is still poorly constrained and may vary with environmental conditions (Stolper et al., 2018). Although, several various models have been developed to simulate the two isotopic tracers $\delta^{18}O$–O_2 and $^{17}\Delta_{\text{ocean}}$ (P. Kroopnick & Craig, 1976; Luz & Barkan, 2000, 2005; Hendricks et al., 2005; Reuer et al., 2007; L. W. Juranek & Quay, 2010; D. P. Nicholson et al., 2012; Munro et al., 2013; D. Nicholson et al., 2014; Palevsky et al., 2016; Li et al., 2022; Musan et al., 2023), none have explored their behavior within a fully coupled global climate framework. This study presents the first climate-model-based investigation of $\delta^{18}O$–O_2 and $^{17}\Delta_{\text{ocean}}$ using iLOVECLIM. The controls on these proxies are examined across different scales, from the large to fine spatial scales, focusing on (1) the influence of environmental variables, (2) the contribution of the main processes, and (3) the role of biological isotopic fractionations.

2 Methods

2.1 iLOVECLIM model

The iLOVECLIM model is an Earth system Model of Intermediate Complexity (EMIC). It was developed from version 1.2 of the LOVECLIM model and retains its main components: atmosphere, ocean, and vegetation (Roche et al., 2007; Goosse et al., 2010).

The atmospheric component, ECBilt, employs a quasi-geostrophic formulation on a T21 spectral grid ($\approx 5.6^\circ$ resolution), with three vertical layers capturing temperature and humidity profiles essential for representing evaporation, precipitation, and condensation (Opsteegh et al., 1998). Ocean circulation is simulated by CLIO, a general circulation model solving the Navier-Stokes equations, thermodynamically coupled to sea ice. It features a $3\times3^\circ$ horizontal resolution, 20 vertical levels, and a free surface to ac-

count for freshwater input from melting glaciers (Goosse & Fichefet, 1999; Goosse et al., 2010). Surface temperature and salinity are updated daily. Advection and diffusion transport tracers throughout the ocean. The oceanic carbon cycle, crucial for representing biological oxygen production, is simulated using a simplified ecosystem model with a single phytoplankton and zooplankton species, along with phosphate as the limiting nutrient (Bouttes et al., 2015). Tracer remineralization follows a depth-dependent profile, capturing the essential dynamics of oxygen and carbon fluxes in the water column.

In a previous study, we added the three stable isotopes of dioxygen ($^{32}O_2$, $^{33}O_2$, $^{34}O_2$) were added to the iLOVECLIM model (Clermont et al., 2026). In order to do so, the main processes affecting oxygen isotopes were explicitly enhanced with their isotopic counterparts: photosynthesis, respiration and ocean-atmosphere gas exchange. In this framework, biological isotopic fractionation factors are prescribed, allowing the distribution of the isotopic tracers $\delta^{18}O$–O_2 and $^{17}\Delta_{ocean}$ to be investigated within a coupled model of intermediate complexity. Unless otherwise stated, the analyses presented in this study are based on a reference control simulation (CTRL), conducted under fixed boundary conditions representative of preindustrial climate. All simulations presented were integrated over 3,000 years, allowing the climate system and isotopic tracers to reach a quasi-equilibrium steady-state.

2.2 Climatological drivers and processes affecting isotopic tracers

Given that these isotopic tracers vary across basins and water masses, large-scale environmental conditions are expected to influence their distribution. To investigate these dependencies, we performed a statistical analysis of the modeled isotopic fields in relation to key environmental variables, using results from the equilibrium control simulation. Dependencies among predictors were assessed using a Spearman correlation matrix. Spearman's rank correlation was chosen because the relationships between environmental variables are not necessarily linear, and several predictors exhibit skewed distributions or contain outliers. Under these conditions, Spearman's correlation provides a robust estimate by capturing monotonic relationships independently of their functional form. To account for potential multicollinearity among predictors, a dimensionality-reduction approach was applied. A Principal Component Analysis (PCA) was performed on the set of environmental variables. The resulting principal components were then used to examine relationships with modeled isotopic tracers, allowing the characterization of dominant large-scale environmental gradients.

In addition to the large-scale statistical analysis, a complementary process-based approach is employed to quantify the contribution of individual physical and biogeochemical mechanisms. The influence of each process on $\delta^{18}O$–O_2 and $^{17}\Delta_{ocean}$ is assessed by isolating their respective contributions.

2.3 Exploration of biological isotopic fractionation coefficients

Following the processes characterization, we turned to the definition of the biological fractionation coefficients required for the oxygen isotopes simulations. These isotopic fractionation coefficients must be defined within the model to represent the distribution of the isotopic tracers $\delta^{18}O$–O_2 and $^{17}\Delta_{ocean}$. The values of these parameters reflect the preferential incorporation of light isotopes during the biological processes of photosynthesis and respiration. The isotopic fractionation coefficient during respiration, denoted as $^{18}\alpha_{resp}$, leads to a depletion in $^{32}O_2$ relative to $^{34}O_2$. Conversely, the fractionation coefficient during photosynthesis, referred to as $^{18}\alpha_{photo}$, results in an enrichment in $^{32}O_2$ relative to $^{34}O_2$. The fractionation coefficients for $^{33}O_2$ are calculated according to the relationship: $^{17}\alpha = \left(^{18}\alpha\right)^{\left(^{17/18}\theta\right)}$.

These parameter values have been estimated in several studies under controlled experimental conditions, for specific locations and species (as summarized in Table 1). $^{18}\alpha_{resp}$ has values reported in the range from 0.9699 to 0.992, with a commonly used value of 0.980 (Kiddon et al., 1993). Earlier studies tended to underestimate the photosynthetic fractionation coefficient, often assuming a value of 1.0 (i.e., no fractionation). However, other work indicates that the coefficient can be significantly higher, with reported values of up to 1.007 (Eisenstadt et al., 2010). The $^{17/18}\theta_{resp}$ coefficient has been shown to vary between 0.516 and 0.5214, with typical values of 0.518 (Helman et al., 2005; L. Juranek & Quay, 2013) or 0.520 (Ash et al., 2020; Li et al., 2022). Finally, the $^{17/18}\theta_{photo}$ coefficient, as $^{18}\alpha_{photo}$, has been measured very few times and published values vary between 0.5198 (Eisenstadt et al., 2010) and 0.5237 (Luz & Barkan, 2011a). All these fractionations coefficients were examined using a set of sensitivity experiments with their values taken in the published ranges and compared with the CTRL reference simulation.

Sensitivity analyses enable us to quantify the influence of individual fractionation factors on tracer distributions. However, the fractionation coefficient values commonly used in models are largely derived from laboratory experiments performed on a limited number of species. As a result, these estimates may not be representative at larger scales or across different oceanic regions. Identifying fractionation values that are appropriate both at the global scale and for specific basins would require running several hundred targeted simulations. To efficiently sample the parameter space while ensuring a robust representation of their distributions, we applied a Latin hypercube sampling strategy to explore four fractionation factors: $^{18}\alpha_{resp}$, $^{17/18}\theta_{resp}$, $^{18}\alpha_{photo}$, $^{17/18}\theta_{photo}$.

3 Applications: Selection of experiments and datasets

3.1 Process deconvolution

The study of large-scale environmental variables was carried out using the CTRL reference simulation. However, five sensitivity simulations were performed to assess the contribution of individual processes to the simulated isotopic tracers. In each experiment, the isotopic effects associated with a single process were selectively suppressed: (i) respiration within the photic zone, (ii) respiration below the photic zone (hereafter referred to as remineralization), (iii) total respiration throughout the ocean, (iv) photosynthesis, and (v) ocean–atmosphere gas exchange.

The contribution of each process was quantitatively estimated as the difference between the corresponding sensitivity simulation and the reference control simulation. Processes that cannot be explicitly isolated, or that act implicitly through the model dynamics, such as ocean circulation, were estimated as the residual between the CTRL simulation and the sum of all explicitly represented processes. This residual term encompasses all remaining physical processes, including ocean circulation, mixing, diffusion, as well as potential non-linear interactions between processes, which are expected to be small.

3.2 Experiments constraining biological isotopic fractionation coefficients

To assess the influence of commonly accepted values for isotopic fractionation processes (Table 1), a set of sensitivity experiments was performed (Table 2). Nine simulations were conducted, in which only a single isotopic fractionation factor was modified at a time. All other fractionation factors were kept identical to those of the reference control simulation, allowing the study of individual impact of each fractionation on the simulated isotopic tracers.

Table 1. Respiratory fractionation factors and theta values for ^{17}O and ^{18}O oxygen isotopologues, modified from Clermont et al., 2026. Nota: The values in brackets correspond to the following model [minimum; maximum]. Values from paper documents prior to the 1970s have not been retained.

Bibliography	$^{18}\alpha_{resp}$	$^{18}\alpha_{photo}$	$^{17/18}\theta_{resp}$	$^{17/18}\theta_{photo}$	Comments
Stevens et al. (1975)	-	[0.9975; 1.003]	-	-	Agmenellum quadruplicatum (blue-green alga)
Stevens et al. (1975)	-	[0.9977; 1.0004]	-	-	Chlorella pyrenoidosa (green alga)
P. M. Kroopnick (1975)	0.9792	-	-	-	Average : marine surface water sample
P. Kroopnick and Craig (1976)	0.9870	-	-	-	Deep Pacific Seawater
Schleser (1979)	0.9820	-	-	-	Average: E.coli
M. L. Bender and Grande (1987)	0.9890	-	-	-	Surface pacific seawater
Guy et al. (1989)	0.9807	-	-	-	Marine diatom
M. L. Bender (1990)	[0.9820; 0.9900]	-	-	-	Deep-sea community respiration
Kiddon et al. (1993)	0.9800 ± 0.003	-	-	-	Marine plankton and bacteria
Quay et al. (1993)	0.9780 ± 0.006	-	-	-	Surface waters of the Subarctic Pacific (measured)
Quay et al. (1993)	[0.9800 ; 0.9880]	-	-	-	Depth waters of the Subarctic Pacific (model)
M. Bender et al. (1994)	0.9800	-	-	-	Estimation according to the Dole Effet
Quay et al. (1995)	0.9820 ± 0.003	-	-	-	Freshwater: rivers and lakes in the Amazon Basin
Luz et al. (2002)	0.9784	-	-	-	Plankton community from Lax Kinneret
Hendricks et al. (2004)	0.9780 ± 0.003	-	-	-	Mixed layer samples from the Southern Ocean
Luz and Barkan (2005)	0.9840	1.0000	0.5179 ± 0.006	-	Experiments on microplankton and bacteria: average
Helman et al. (2005)	-	-	0.518 ± 0.001	0.5260	Experiments respiration
Hendricks et al. (2005)	0.9790 ± 0.002	-	-	-	Upper column from the equatorial Pacific
Levine et al. (2009)	0.9920	-	-	-	Mesopelagic ocean in diapycnal model
Eisenstadt et al. (2010)	-	1.0030	0.5180	0.5253 ± 0.0004	Nannochloropsis sp. (Eustigmatophyceae)
Eisenstadt et al. (2010)	-	1.0070	-	0.5198 ± 0.0001	Green algae (Chlamydomonas reinhardtii)
Eisenstadt et al. (2010)	-	1.0045	-	0.5234 ± 0.0004	Diatoms (Phaeodactylum tricornutum)
Eisenstadt et al. (2010)	-	1.0055	-	0.5253 ± 0.0004	Coccolithophores (Emiliania huxleyi)
Luz and Barkan (2011b)	-	1.0034	0.5160	0.5237	Theory
Luz and Barkan (2011a)	0.9803	1.0040	-	-	Average marine in surface ocean
Luz and Barkan (2011a)	0.9733	1.0054	-	-	Southern Ocean, with Fe addition
Luz and Barkan (2011a)	0.9731	1.0057	-	-	Southern Ocean, without Fe addition
Luz and Barkan (2011a)	0.9740	1.0042	-	-	Celtic Sea, bloom
Luz and Barkan (2011a)	0.9728	1.0034	-	-	Celtic Sea, prebloom
Luz and Barkan (2011a)	0.9772	1.0026	-	-	N. Atlantic near Bermuda
Luz and Barkan (2011a)	0.9780	1.0020	-	-	Red Sea near Eilat
Luz and Barkan (2011a)	-	-	-	0.5370	Cyanobacteria from Helmann et al., 2005
L. Juranek and Quay (2013)	-	-	0.5180	-	Review
Ash et al. (2020)	0.9800	-	0.5200	-	Lake Houston's Deussen Park
Wurgaft et al. (2022)	0.9755	-	-	-	Red Sea (incubation experiment)
Wurgaft et al. (2022)	0.9860	-	-	-	Red Sea (in situ)
Li et al. (2022)	0.9890	-	0.5200	-	Model for Deep Northeast Pacific Ocean
Sutherland et al. (2022)	0.9880 ± 0.004	-	0.5214 ± 0.0004	-	Marine heterotrophs organisms
Bienville et al. (2026)	0.9699	1.0050	-	-	Marine algae (25 °C)

Fractionation coefficient factor during respiration $^{18}\alpha_{resp}$ was explored through 4 simulations. The first tests the effect of a high fractionation coefficient ($^{18}\alpha_{resp} = 0.9699$), derived from a new experiment conducted by Bienville et al. (2026). In an effort to obtain fractionation factors values as coherent with real ecosystems as possible, Bienville et al. (2026) have developed an intermediary scale setup where they measured the isotope fractionations associated with photosynthesis and respiration of a phytoplankton community in water at 25°C. Fractionation coefficients with values of 0.982 and 0.988 on the other hand represent more commonly accepted values: 0.982 corresponds to an estimated average for overall fractionation in freshwater environments (Quay et al., 1995), whereas 0.988 reflects a smaller fractionation potentially occurring in deep waters (Quay et al., 1993).

In addition, the "Stolper: f(T)" sensitivity test corresponds to a temperature-dependent fractionation model based on bacterial respiration experiments (Stolper et al., 2018). The temperature functions implemented in the iLOVECLIM model, taken from (Stolper et al., 2018), are as follow:

$$^{18}\alpha_{\text{resp}} = \frac{1000 - (0.11\,T + 12.7)}{1000} \tag{2}$$

$$^{17/18}\theta_{\text{resp}} = 2.1 \times 10^{-4}\,T + 0.5054 \tag{3}$$

To evaluate the influence of $^{17/18}\theta_{resp}$, three additional simulations were carried out. The first one used a value ($^{17/18}\theta_{resp} = 0.515478$) for which, given a respiration fractionation factor of 0.980, the $^{17}\Delta_{\text{ocean}}$ remains unaffected by respiration. The two other simulations bracket the control value (0.518) with 0.516 and 0.520, allowing the impact of $^{17/18}\theta_{resp}$ variations to be quantified. The latter (0.520) is also consistent with recent values published in the literature (Ash et al., 2020; Li et al., 2022).

In order to explore the influence of isotopic effect during photosynthesis, two additional sensitivity tests of $^{18}\alpha_{photo}$ were performed. Although this process was long considered negligible, other studies have revealed measurable fractionation effects, with reported values around 1.004 (Eisenstadt et al., 2010). Bienville et al. (2026) further determined a slightly higher fractionation coefficient, close to 1.005. Both values (1.004 and 1.005) were therefore implemented in the model as sensitivity tests to evaluate the potential influence of photosynthetic fractionation. In these simulations, the $^{17/18}\theta_{photo}$ for photosynthesis was kept constant at 0.520, consistent with values generally observed for mass-dependent processes.

Table 2. List of nine sensitivity tests to explore the fractionation coefficients. CTRL corresponds to the reference simulation. Simulation names indicate the modified parameter.

Simulation name	$^{18}\alpha_{\text{resp}}$	$^{17/18}\theta_{\text{resp}}$	$^{18}\alpha_{\text{photo}}$
CTRL	0.980	0.518	1.0
$^{18}\alpha_{\text{resp}} = 0.9699$	0.9699	–	–
$^{18}\alpha_{\text{resp}} = 0.982$	0.982	–	–
$^{18}\alpha_{\text{resp}} = 0.988$	0.988	–	–
Stolper: $f(T)$	$f(T)$	$f(T)$	–
$^{17/18}\theta_{\text{resp}} = 0.515478$	–	0.515478	–
$^{17/18}\theta_{\text{resp}} = 0.516$	–	0.516	–
$^{17/18}\theta_{\text{resp}} = 0.520$	–	0.520	–
$^{18}\alpha_{\text{photo}} = 1.004$	–	–	1.004
$^{18}\alpha_{\text{photo}} = 1.005$	–	–	1.005

3.3 Latin Hypercube method and in situ observations

The combination of the four fractionations were investigated using 300 simulations carried out with the Latin Hypercube method. Each simulation corresponding to a unique combination of fractionation coefficients within the ranges reported in the literature (Table 1). For respiration, $^{18}\alpha_{\text{resp}}$ varied between 0.9699 to 0.9920, while $^{17/18}\theta_{\text{resp}}$ ranged from 0.5160 to 0.5214. For photosynthesis, $^{18}\alpha_{\text{photo}}$ ranged from 1.000 to 1.007, and $^{17/18}\theta_{\text{photo}}$ from 0.5198 to 0.537. For each simulation, the Root Mean Square Error (RMSE) was computed by comparing the modeled tracer fields to in situ measurements, using the nearest model grid point at each observation location (longitude, latitude, and depth). Model–data misfit was quantified using a normalized RMSE combining both δ^{18}O–O_2 and $^{17}\Delta_{\text{ocean}}$, ensuring that both proxies contribute equally to the total score.

2,482 measurement points were compiled from the literature, mostly obtained during oceanographic campaigns. Oxygen concentrations were measured either using sensors mounted on CTD rosettes or from discrete bottle samples. δ^{18}O–O_2 and $^{17}\Delta_{\text{ocean}}$ are therefore available across ocean basins at different depths. In the Atlantic Ocean, data from Luz and Barkan (2009), Levine et al. (2009), Yeung et al. (2012) and Musan et al. (2023) were included, complemented by Bermuda Atlantic Time-series measurement stations (BAT; Johnson et al. (2025)). In the Pacific Ocean, data from Hendricks et al. (2005), Sarma et al. (2008), L. W. Juranek et al. (2012), Palevsky et al. (2016) and Li et al. (2022) were used, along with measurements from the Hawaiian Ocean Time-series (HOT; Argo (2025)) station. For the Southern Ocean, we compiled datasets from Hendricks et al. (2004), Reuer et al. (2007), Huang et al. (2012), Castro-Morales et al. (2013) and M. L. Bender et al. (2016), all obtained during the austral summer and from subsurface waters ($>$ 100 m). And finally, we recovered only a few points in the Arctic Ocean, originating from Stanley et al. (2015). Where needed, we recalculated $^{17}\Delta_{\text{ocean}}$ from original data to ensure that all dataset uses a consistent definition. Because these observations are spatially discrete, the upper 100 meters are grouped into a single "photic layer" which is often influenced by strong seasonal variability and biological activity.

4 Results and discussion

4.1 Large-scale climatic controls on isotopic tracers

Although seasonal variability influences isotopic tracers at local scales, the role of climatological parameters was assessed using Spearman's correlation to identify the dominant controls on their distributions (Figure 1).

Spearman's correlation revealed several perfect relationships among predictors ($p = 1$), notably between δ^{18}O–O_2 and δ^{17}O–O_2 or among O_2 and its isotopologues ($^{32}O_2$, $^{33}O_2$, $^{34}O_2$). These redundancies reflect the same processes expressed through different variables. To reduce dimensionality in the heatmap, δ^{18}O–O_2 and δ^{17}O–O_2 were combined into a single variable (δ^*O–O_2). Isotopologues of O_2 were excluded as they are intrinsically linked within the same molecule and therefore do not provide additional independent information. Nitrate and phosphate were grouped under "nutrients" given their identical behavior. The resulting correlation matrix preserves the essential relationships among variables while eliminating redundant information (Figure 1). Three coherent groups of predictors emerge from this structure: a biological group including phytoplankton, Net Community Production (NCP), remineralization and O_2; a chemical group including Dissolved Organic Carbon (DOC), slow Dissolved Organic Carbon (DOCs), Dissolved Inorganic Carbon (DIC), nutrients; and a hydrographic group composed of temperature, salinity and oxygen saturation. These three groups structure the environmental space in which isotopic tracers evolve. The triple isotopic composition of dissolved oxygen is positively correlated with δ^*O–O_2 ($p = 0.7$). Notably, these tracers shows any association with salinity. This reflects the fact that oxygen isotope composition of sea-

water in the model is prescribed to VSMOW values rather than to the isotopic composition of seawater itself, a simplification that prevents the model from reproducing the relationship between the salinity and δ^*O–O_2.

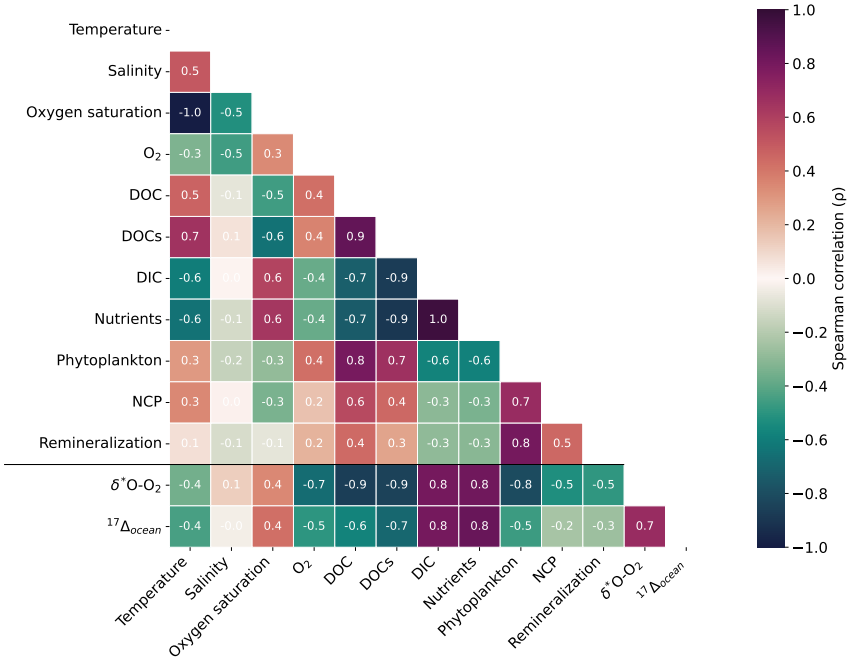

Figure 1. Spearman's correlation matrix. The line separates predictors from isotopic tracers. δ^*O–O_2 corresponds to δ^{18}O–O_2 and δ^{17}O–O_2. Nutrients combined the nitrate and phosphate variables. Acronym: DOC = Dissolved Organic Carbon; DOCs = slow Dissolved Organic Carbon; DIC = Dissolved Inorganic Carbon; NCP = Net Community Production

To complement these results, a principal component analysis was conducted on the predictor variables. The first three components account for 82% of the total variance, with PC1, PC2 and PC3 explaining 45.8%, 21.2% and 15.0%, respectively. The biplot displays the projection of variables onto the first two principal axes (Figure 2). PC1 captures the dominant biogeochemical gradient, opposing warm surface waters enriched in DOC to deeper waters enriched in nutrients and DIC. This pattern reflects the balance between biological production and nutrient concentrations along the vertical gradient. PC2 represents a secondary mode of variability related to oxygen dynamics, contrasting elevated O_2 concentration with hydrographic properties, particularly salinity and temperature. The biplot also reveals covariation patterns among variables, as indicated by vector angles. DIC and nutrients exhibit strong positive covariance, while phytoplankton, O_2 and NCP covary as components of the oxygen cycle. Overall, the PCA supports the grouping of predictors into three main processes: physical, biological and chemical, consistent with the correlation analysis (Figure 1).

Finally, the regression analysis yields an r^2 of 0.72 for δ^*O–O_2 and 0.58 for $^{17}\Delta_{\text{ocean}}$, indicating that δ^*O–O_2 variability is more strongly explained by the leading environmental modes than $^{17}\Delta_{\text{ocean}}$. These results highlight a systematic difference in the environmental controls on the two tracers. δ^*O–O_2 variability is aligned with the dominant environmental gradients captured by the PCA, making it a broadly integrative tracer of the ocean's biogeochemical state. In contrast, $^{17}\Delta_{\text{ocean}}$ is more sensitive to local imbalances between oxygen production, consumption and air-sea exchange. These processes

may deviate from large-scale patterns and are therefore less well represented in the dominant modes of environmental variability. The lower r^2 for $^{17}\Delta_{ocean}$ thus reflects its sensitivity to process-level oxygen cycle dynamics.

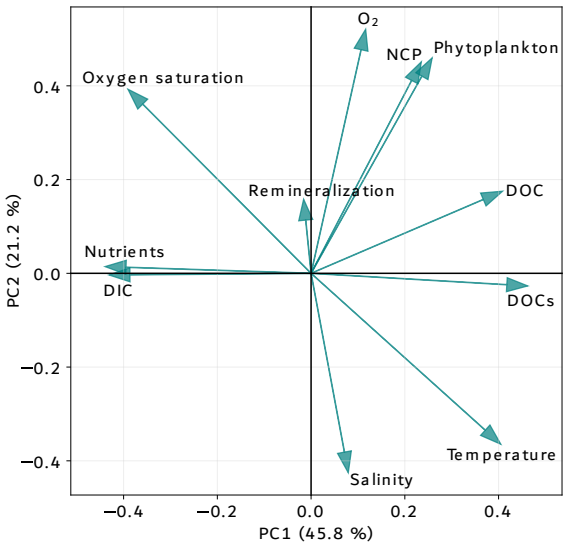

Figure 2. Principal component (PC) analysis on the predictors. Please refer to Figure 1 for the acronyms.

Together, these two tracers are complementary: $\delta^*O–O_2$ captures the large-scale structure of environmental variability, while $^{17}\Delta_{ocean}$ provides additional constraints on oxygen cycle imbalances at the process level. To further disentangle the respective contributions of these mechanisms, a process-based decomposition is performed in the following section.

4.2 Intermediate-scale process-driven variability of isotopic signals

While environmental variables provide a first-order control on proxy distributions, these factors act through distinct physical and biological mechanisms. The $\delta^{18}O–O_2$ and $^{17}\Delta_{ocean}$ signals are deconvolved to quantify the respective contributions of the main governing processes: photosynthesis, respiration and air-sea gas exchange. The remaining isotopic signal is then attributed to broader physical processes, such as ocean circulation and diapycnal mixing, which integrate the transport-related drivers of the distribution (Figure 3).

Overall, both isotopic proxies exhibit highest values in the subsurface, but respond differently to the underlying processes (Figure 3). For $\delta^{18}O–O_2$, elevated values are primarily driven by remineralization (Figure 3a), with total respiration contributing increases of up to 12‰. Physical processes also contribute positively to the $\delta^{18}O–O_2$ signal, whereas photosynthesis is the only process inducing a substantial decrease, reaching values as low as -9‰. In contrast, for $^{17}\Delta_{ocean}$ all biological processes contribute positively to the signal (Figure 3b). Photosynthesis is the dominant control and can increase $^{17}\Delta_{ocean}$ by up to 40 ppm. Only physical processes result in a decrease in $^{17}\Delta_{ocean}$ signal. As a result, photosynthesis and physical processes exert opposite effects on the two isotopic prox-

ies. Photosynthesis remains the most decisive process determining δ^{18}O–O_2 and $^{17}\Delta_{ocean}$ values for the global ocean.

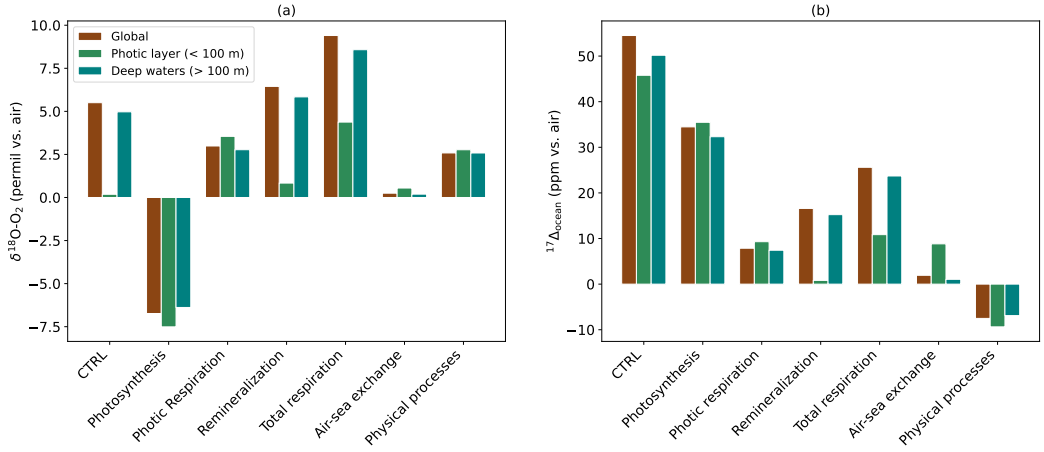

Figure 3. Deconvolution of the isotopic signals for (a) δ^{18}O–O_2 and (b) $^{17}\Delta_{ocean}$. Results are shown for three depth categories: brown indicates the ocean-wide average, the photic layer represents the mean over the upper 100 m (green), and deep waters corresponds to waters below 100 m (blue). CTRL denotes the reference simulation including all processes. Total respiration integrates respiration over the entire water column and includes respiration in the photic zone ("Photic respiration") as well as subsurface respiration associated with organic matter degradation and bacterial activity ("Remineralization"). This vertical partitioning is imposed by the iLOVECLIM model structure; however, respiration and remineralization occur in both layers in reality, making "Total respiration" the most physically representative quantity. Physical processes represent the residual signal. It can be attributed to circulation and mixing, and are calculated as CTRL minus the explicitly deconvolved processes.

A limitation of the iLOVECLIM model is that photosynthesis and photic respiration are restricted to the upper 100 m, whereas in reality their vertical extent depends on ocean structure and light penetration. Despite this imposed depth limitation, the isotopic signals generated by these processes are transported to greater depths through mixing and transport. This subsurface accumulation of $^{17}\Delta_{ocean}$ is consistent with the observational and modeling results from the Pacific reported by Hendricks et al. (2005). At these depths, accumulation occurs because the signal is no longer regulated by ocean-atmosphere exchange, which tends to restore the proxies to equilibrium. Moreover, the patterns observed in the Pacific agree with our deconvolution: respiration induces an increase in δ^{18}O–O_2, whereas photosynthesis induces a decrease in δ^{18}O–O_2 and an increase in $^{17}\Delta_{ocean}$.

It should be noted that these results are obtained with the CTRL simulation, which employs prescribed fractionation coefficients for the biological and physical processes considered. Under this parameterization, the chosen fractionation values introduce a non-negligible sensitivity of $^{17}\Delta_{ocean}$ to respiration (Figure 3b). This behavior departs from the classical definition proposed by (Luz & Barkan, 2005), in which $^{17}\Delta_{ocean}$ is assumed to be insensitive to respiration. This sensitivity highlights the importance of accurately constraining isotope fractionation coefficients and their associated uncertainties when interpreting oxygen isotopic tracers.

4.3 Fine-scale influence and constraints of biological isotopic fractionation

In the iLOVECLIM model, biological isotope fractionation coefficients are prescribed based on estimates from the literature (Table 1). These fractionation coefficients may vary depending on species composition, geographical region, depth, and environmental conditions. However, in the iLOVECLIM model, a representative prescribed value for the global ocean is assumed for each biological fractionation process occurring during photosynthesis ($^{18}\alpha_{\text{photo}}$, $^{17/18}\theta_{\text{photo}}$) and respiration ($^{18}\alpha_{\text{resp}}$, $^{17/18}\theta_{\text{resp}}$). The sensitivity of the simulated isotopic signal to these parameters was investigated through a set of sensitivity experiments in which each fractionation factor was varied independently, to quantify its specific impact on the proxies (Figure 4).

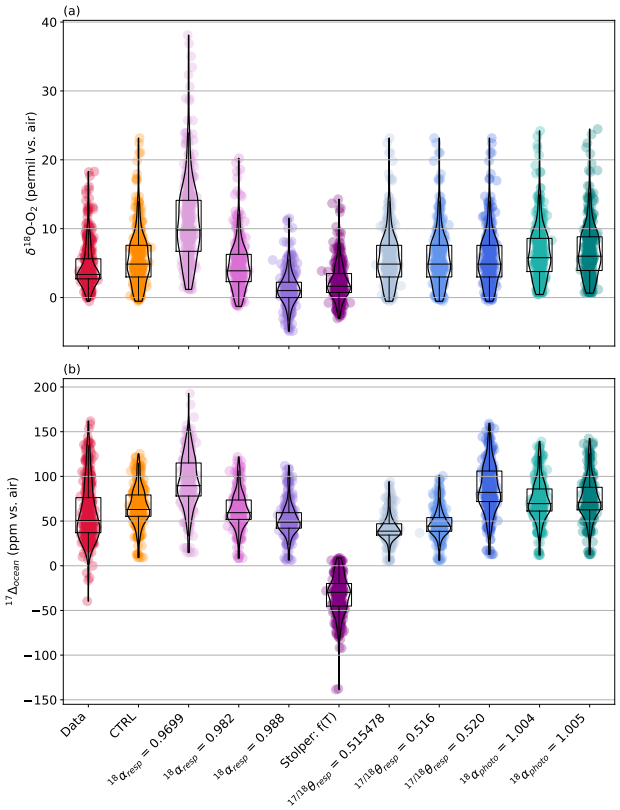

Figure 4. Sensitivity tests of biological fractionation coefficients for (a) δ^{18}O–O_2 and (b) $^{17}\Delta_{\text{ocean}}$. Red points indicate observational data, for which model–data comparisons were performed at matching longitude, latitude, and depth. Colors denote the processes investigated: $^{18}\alpha_{\text{resp}}$ (pink-purple), $^{17/18}\theta_{\text{resp}}$ (blue), and $^{18}\alpha_{\text{photo}}$ (green). See Table 2 for further details.

Respiration induces two contrasting effects on the isotopic proxies. A weaker respiratory isotope fractionation (i.e., greater $^{18}\alpha_{\text{resp}}$ value) leads to a decrease in both δ^{18}O–O_2 and $^{17}\Delta_{\text{ocean}}$. In contrast, an increase of $^{17/18}\theta_{\text{resp}}$ value results in an increase in $^{17}\Delta_{\text{ocean}}$, while this does not affect δ^{18}O–O_2. In contrast, the photosynthetic isotope fractionation $^{18}\alpha_{\text{photo}}$, induces an increase in both δ^{18}O–O_2 and $^{17}\Delta_{\text{ocean}}$. However, modifying $^{18}\alpha_{\text{photo}}$ by + 0.001 does not produce any significant change in either proxy, suggesting a weak sensitivity of the simulated isotopic signal to this parameter within the tested range.

The "Stolper simulation", which incorporates temperature-dependent isotope fractionation effect during respiration, reproduces $\delta^{18}O–O_2$ relatively well compared to the data but fails to capture the observed values of $^{17}\Delta_{ocean}$. Several factors may explain this discrepancy. First, the temperature dependence used in this parameterization is derived from experiments conducted on a single heterotrophic bacterium (E. coli). Second, these experiments were performed over a limited temperature range (10 - 40 °C), which is not representative of the full range of environmental conditions relevant at the global ocean scale simulated by iLOVECLIM.

Overall, the simulations that best reproduce both $\delta^{18}O–O_2$ and $^{17}\Delta_{ocean}$ are the CTRL and the experiment using $^{18}\alpha_{resp} = 0.982$. These results suggest that a value of $^{17/18}\theta_{resp} = 0.518$ provides the most appropriate representation within the current model framework among the tested values. In contrast, the tested photosynthetic fractionation coefficient alone does not lead to an improved agreement with the data. Nevertheless, each fractionation factor exerts a distinct influence on the simulated proxies, highlighting the sensitivity of $\delta^{18}O–O_2$ and $^{17}\Delta_{ocean}$ to biological parameter choices.

4.4 Improving the parametrization of biological isotopic fractionation in the global ocean

Given the variability of fractionation factors across species and environments, assigning a single value to each process necessarily introduces assumptions and uncertainties. To further constrain the parameter space and reduce these uncertainties, 300 additional simulations were performed using a Latin hypercube sampling approach based on published ranges from the literature (Table 1). This strategy allows for a more systematic exploration of the combined effects of biological fractionation coefficients and provides a basis for identifying the most robust model parameterizations. These 300 simulations were analyzed, and for each spatial location (global ocean, photic layer, deep ocean), the 10 parameter combinations yielding the lowest total RMSE in comparison to the observational data were retained for further analysis (Figure 5). Hence, the average of the 10 best simulations was calculated for each zone, yielding the best combinations of parameters (Table 3).

Table 3. Average of the 10 best simulations for each location. The photic layer describes the top 100 meters of the ocean, while the deep ocean corresponds to depths greater than 100 meters.

		Respiration		Photosynthesis	
Region	Layer	$^{18}\alpha_{resp}$	$^{17/18}\theta_{resp}$	$^{18}\alpha_{photo}$	$^{17/18}\theta_{photo}$
CTRL		0.980	0.518	1.000	0.520
Global	All	0.983	0.517	1.002	0.524
	Photic layer	0.982	0.517	1.003	0.524
	Deep ocean	0.985	0.517	–	–
Atlantic	All	0.987	0.517	1.005	0.526
	Photic layer	0.980	0.520	1.005	0.533
	Deep ocean	0.988	0.517	–	–
Pacific	All	0.981	0.517	1.002	0.526
	Photic layer	0.979	0.517	1.002	0.527
	Deep ocean	0.982	0.517	–	–
Arctic	All	0.983	0.517	1.003	0.525
	Photic layer	0.982	0.517	1.003	0.525
	Deep ocean	0.984	0.517	–	–
Southern	All	0.982	0.517	1.003	0.525
	Photic layer	–	–	–	–
	Deep ocean	–	–	–	–

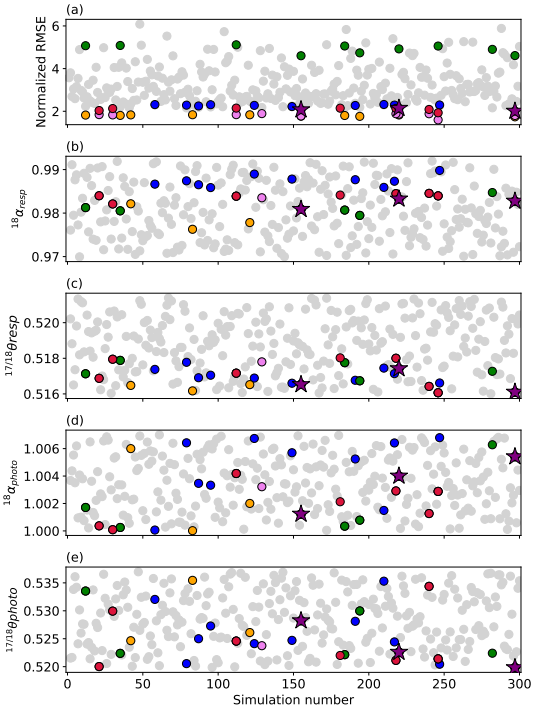

Figure 5. Top 10 simulations by ocean basin. Red, blue, orange, green, and pink dots indicate the best simulations for the global, Atlantic, Pacific, Southern, and Arctic Oceans, respectively. Stars denote simulations that perform best across multiple basins (global, Pacific, Arctic, and Southern), excluding the Atlantic.

4.4.1 Global ocean

In the iLOVECLIM model, biological fractionation coefficients are prescribed uniformly across the global ocean. This section assesses the validity of this assumption by analyzing the optimal parameter combinations identified for the global ocean.

Figure 5 summarizes the distribution of fractionation coefficients among the simulations yielding the lowest normalized RMSE values. At the global scale, the RMSE values associated with the best-performing simulations are generally low, indicating that a satisfactory agreement with the observational constraints can be achieved. For the respiration process, the optimal parameter combinations cluster within a relatively narrow range, with $^{18}\alpha_{\mathrm{resp}}$ values between 0.979 and 0.988 and $^{17/18}\theta_{\mathrm{resp}}$ values close to 0.517 (see Figure 5b; Figure 5c; Table 3). In contrast, no clear clustering emerges for the photosynthetic fractionation coefficients, suggesting a weaker constraint on these processes at the global scale (Figures 5d; 5e).

Overall, these results indicate that no single optimal value can be identified independently for each fractionation coefficient. Instead, the simulations point toward sets of parameter values that jointly provide a good representation of both $\delta^{18}\mathrm{O}$–O_2 and $^{17}\Delta_{\mathrm{ocean}}$. The mean parameter values derived from the 10 best global simulations (Table 3) highlight a vertical contrast between the photic and deep ocean, particularly for the $^{18}\alpha_{\mathrm{resp}}$. The magnitude of this respiratory fractionation decreases with depth (or $^{18}\alpha_{\mathrm{resp}}$ value increases), whereas the $^{17/18}\theta_{\mathrm{resp}}$ value remains mostly homogeneous throughout the water column. To further explore the characteristics of the best-performing parameter sets for the global ocean, the 10 simulations with the lowest RMSE value were analyzed in

detail. Statistical metrics were computed for different depth domains: global ocean, photic layer, and deep ocean (Table 4).

Table 4. Analysis of the 10 best simulations for the global ocean. The photic layer describes the top 100 meters of the ocean, while the deep ocean corresponds to depths greater than 100 meters.

		Respiration		Photosynthesis	
		$^{18}\alpha_{\text{resp}}$	$^{17/18}\theta_{\text{resp}}$	$^{18}\alpha_{\text{photo}}$	$^{17/18}\theta_{\text{photo}}$
All ocean	Best simulation (No. 246)	0.984	0.516	1.003	0.521
	Average	0.983	0.517	1.002	0.524
	Standard deviation	0.001	0.001	0.002	0.005
	Confidence interval (95%)	0.001	0.001	0.001	0.003
	Correlation between parameters	0.14		-0.50	
Photic layer	Best simulation (No. 297)	0.983	0.516	1.005	0.520
	Average	0.982	0.517	1.003	0.524
	Standard deviation	0.002	0.001	0.002	0.005
	Confidence interval (95%)	0.001	0.001	0.002	0.003
	Correlation between parameters	-0.22		-0.45	
Deep ocean	Best simulation (No. 217)	0.987	0.517	–	–
	Average	0.985	0.517	–	–
	Standard deviation	0.001	0.001	–	–
	Confidence interval (95%)	0.001	0.001	–	–
	Correlation between parameters	0.33	–	–	–
	Correlation between parameters	0.33			

Across all depth domains, confidence intervals are very narrow for all fractionation coefficients, especially for the respiration-related parameters ($^{18}\alpha_{\text{resp}}$ and $^{17/18}\theta_{\text{resp}}$), indicating that they are strongly constrained (Table 4). The analysis of parameter correlations yields consistent patterns across all depth domains. For photosynthetic fractionations, a moderate negative correlation ($\pm$ -0.5) is observed between $^{18}\alpha_{\text{photo}}$ and $^{17/18}\theta_{\text{photo}}$, indicating that the model requires a specific magnitude of $^{17}\Delta_{\text{ocean}}$ in photosynthetic O_2, such that a higher alpha is associated with a lower theta value and vice versa. This is consistent with triple oxygen isotope systematics (e.g., Luz and Barkan (2000)): photosynthetic O_2 inherits the isotopic composition of the source water (VSMOW in our case), imposing a coupled relationship between $^{18}\alpha_{\text{photo}}$ and $^{17/18}\theta_{\text{photo}}$. In contrast, respiration-related fractionations exhibit negligible correlation, indicating that $^{18}\alpha_{\text{resp}}$ and $^{17/18}\theta_{\text{resp}}$ can be adjusted independently without affecting model performance.

Consistent with these correlation patterns, respiration-related fractionation coefficients are tightly constrained and exhibit very limited variability across the best-performing simulations (coefficient of variation $\pm$ 0.001). The global ocean mean value of $^{18}\alpha_{\text{resp}}$ is 0.983, with an average value of 0.982 at the surface and a reduced fractionation at depth to 0.985. To further constrain this parameter, we examined the simulation minimizing the RMSE of $\delta^{18}O$–O_2, which is only sensitive to the $^{18}\alpha_{\text{resp}}$. Consistent with the previous value, we obtained a deep ocean value of 0.986. These estimates of respiration-related fractionation are in good agreement with previous deep oceanic observations (M. L. Bender, 1990; Quay et al., 1993), thereby reinforcing the robustness of our model. Furthermore, $^{17/18}\theta_{\text{resp}}$ remains tightly constrained, with value close to 0.517 across the global ocean. This estimate is closest to the value reported by Luz and Barkan (2005), although it remains slightly higher, which may reflect the fact that their estimate was derived from laboratory experiments on microplankton and bacteria. In contrast, more recent studies have suggested systematically higher values (0.520–0.521), which are not supported by our model results.

Photosynthetic fractionation coefficients display greater flexibility, particularly $^{17/18}\theta_{\text{photo}}$, whose variability is acceptable as long as its covariation with $^{18}\alpha_{\text{photo}}$ is preserved. The values of the photosynthetic fractionations, for both $^{18}\alpha_{\text{photo}}$ and $^{17/18}\theta_{\text{photo}}$, are consistent with the measured values (Eisenstadt et al., 2010; Luz & Barkan, 2011b). Because these two fractionations are intrinsically linked, they can vary over a relatively broad range while producing comparable model performance. This behavior allows a robust estimation of the photosynthetic isotopic signal from their combined values. For the global ocean, the inferred optimal $^{17}\Delta_{\text{ocean}}$ signature of photosynthetic O_2 is 226 ppm.

Overall, these results confirm that respiration fractionation coefficients occupy a narrowly defined and well-constrained region of the parameter space, whereas photosynthetic fractionations span a broader range constrained primarily by internal consistency rather than by individual optimal values. This highlights that accurately reproducing δ^{18}O–O_2 and $^{17}\Delta_{\text{ocean}}$ requires coherent combinations of fractionation coefficients rather than a single best estimate for each process. It should also be noted that these conclusions reflect the optimal parameter space explored within the tested ranges and the current model framework.

4.4.2 Ocean basins

Across the 300 simulations, respiration-related fractionation coefficients remain tightly constrained in all basins, whereas photosynthetic fractionation coefficients exhibit greater variability (Table 3; Table 4). A systematic decrease of $^{18}\alpha_{\text{resp}}$ with depth is observed in all basins, with values ranging from 0.979 to 0.988. In contrast, $^{17/18}\theta_{\text{resp}}$ remains remarkably stable and close to 0.517, except in the Atlantic photic layer. Photosynthetic fractionation coefficient span a broader range of values, with $^{18}\alpha_{\text{photo}}$ varying between 1.002 and 1.005 and $^{17/18}\theta_{\text{photo}}$ between 0.524 and 0.533, reflecting a comparatively larger range of admissible values in the model.

For the global ocean, the parameter combination yielding the lowest RMSE corresponds to simulation n°246 (Table 4). Although each basin exhibits variations in fractionation, particularly along the water column for $^{18}\alpha_{\text{resp}}$, this simulation provides the best overall fit for the global ocean. Consistent with the respective roles of the different fractionation processes, simulation 246 is associated with an overall decrease in δ^{18}O–O_2 relative to the CTRL simulation, accompanied by a more complex response in $^{17}\Delta_{\text{ocean}}$ (see Table 3; Figure 4; Figure A1), reflecting the opposing influences of respiration and photosynthesis fractionations. Simulation 246 reproduces these basin-scale patterns with more moderate amplitudes, consistent with its role as a compromise parameterization designed to provide an adequate representation across multiple ocean basins.

Figure 6 shows the measured versus modelled points from simulation 246 in the Atlantic and Pacific Oceans. Both δ^{18}O–O_2 and $^{17}\Delta_{\text{ocean}}$ exhibit comparable ranges of variability across these two basins, and the model reproduces large-scale spatial patterns with reasonable ranges. In the Atlantic Ocean, δ^{18}O–O_2 ranges from -2 to 20‰ in both observed and modelled datasets (Figure 6a). The highest values are found within the upper water column, whereas in the deep ocean δ^{18}O–O_2 stabilizes around 3‰ in the observations and 5‰ in the model. This vertical structure is consistent with the confinement of biological activity to the photic zone, leading to enhanced variability near the surface and more homogeneous conditions at depth. A similar vertical structure is observed for $^{17}\Delta_{\text{ocean}}$. Surface values range from 0 to 150 ppm in the observations, compared to 0 to 90 ppm in the model. At depth, observed $^{17}\Delta_{\text{ocean}}$ exhibits variability within a narrower range of 30 to 60 ppm, whereas the model produces a nearly uniform value around 50 ppm. The reduced surface variability in the model likely reflects the use of compromise fractionation coefficients in simulation 246, which differ from those of the best-performing simulation in the Atlantic (Table 3).

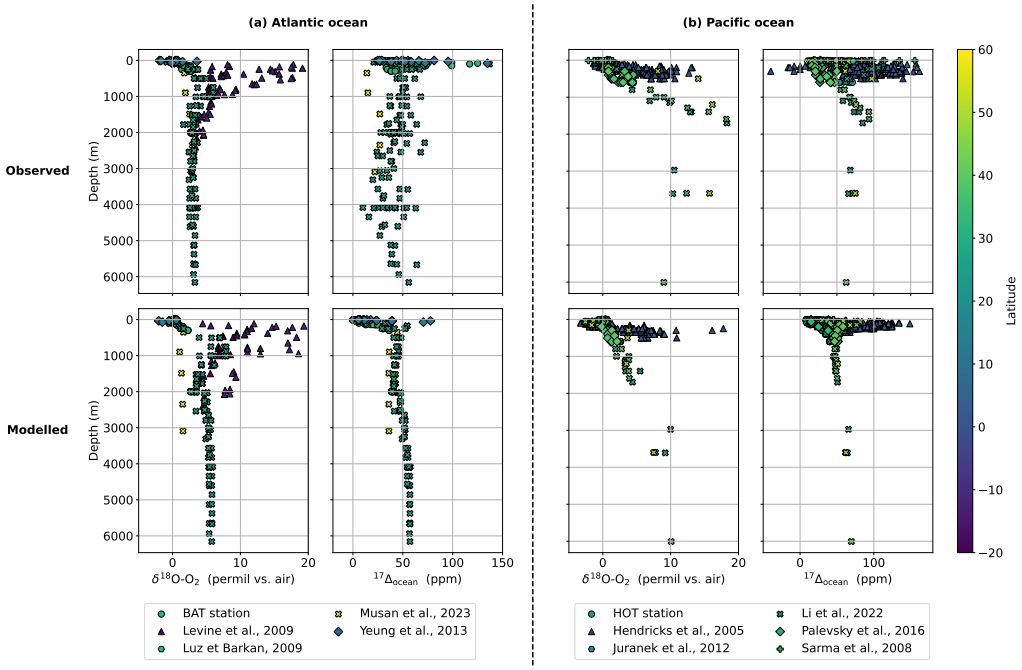

Figure 6. Analysis of δ^{18}O–O$_2$ and $^{17}\Delta_{\text{ocean}}$ from measured (top panels) and modelled data (bottom panels) using the best combination for the global ocean, i.e. simulation n°246. Panels (a) and (b) correspond to the Atlantic and Pacific Oceans, respectively. Modelled points are extracted at the locations of the observations and account for seasonal variability.

In the Pacific Ocean, a similar vertical structure is observed, although deep-water data remain more limited (Figure 6b). The largest variations in both δ^{18}O–O$_2$ and $^{17}\Delta_{\text{ocean}}$ occur within the upper 300 meters, followed by a progressive stabilization throughout the water column. For δ^{18}O–O$_2$, values range from -2 to 20‰ in both observations and simulations, with deep-water values stabilizing around 15‰ in the observations and 10‰ in the model. For $^{17}\Delta_{\text{ocean}}$, observed values span from -45 to 160 ppm, whereas the model simulates a slightly narrower range of 0 to 150 ppm, converging toward 60 ppm at depth. This agreement extends to the Arctic Ocean (Figure B1), while the Southern Ocean emerges as a notable exception (Figure B2).

The Southern Ocean exhibits systematically higher RMSE values than other basins (Figure 5), reflecting a persistent model bias associated with excessive phytoplankton activity. This leads to enhanced photosynthetic rates and, consequently, to an overestimation of the $^{17}\Delta_{\text{ocean}}$ signal (Figure 3, Figure B2). While compensating processes such as respiration may partly offset this imbalance in terms of bulk oxygen or carbon fluxes, they do not correct the isotopic signature, thereby amplifying the bias in $^{17}\Delta_{\text{ocean}}$. An additional experiment, motivated by differences identified in other models, was performed in which phytoplankton biomass was reduced by 50% in the Southern Ocean as an idealized perturbation to assess the impact on simulated isotopic tracers and model–data misfit. Model performance was then evaluated using linear regressions between simulated and observed δ^{18}O–O$_2$ and $^{17}\Delta_{\text{ocean}}$ for the CTRL simulation, simulation 246, and this reduced-phytoplankton experiment (Figure 7).

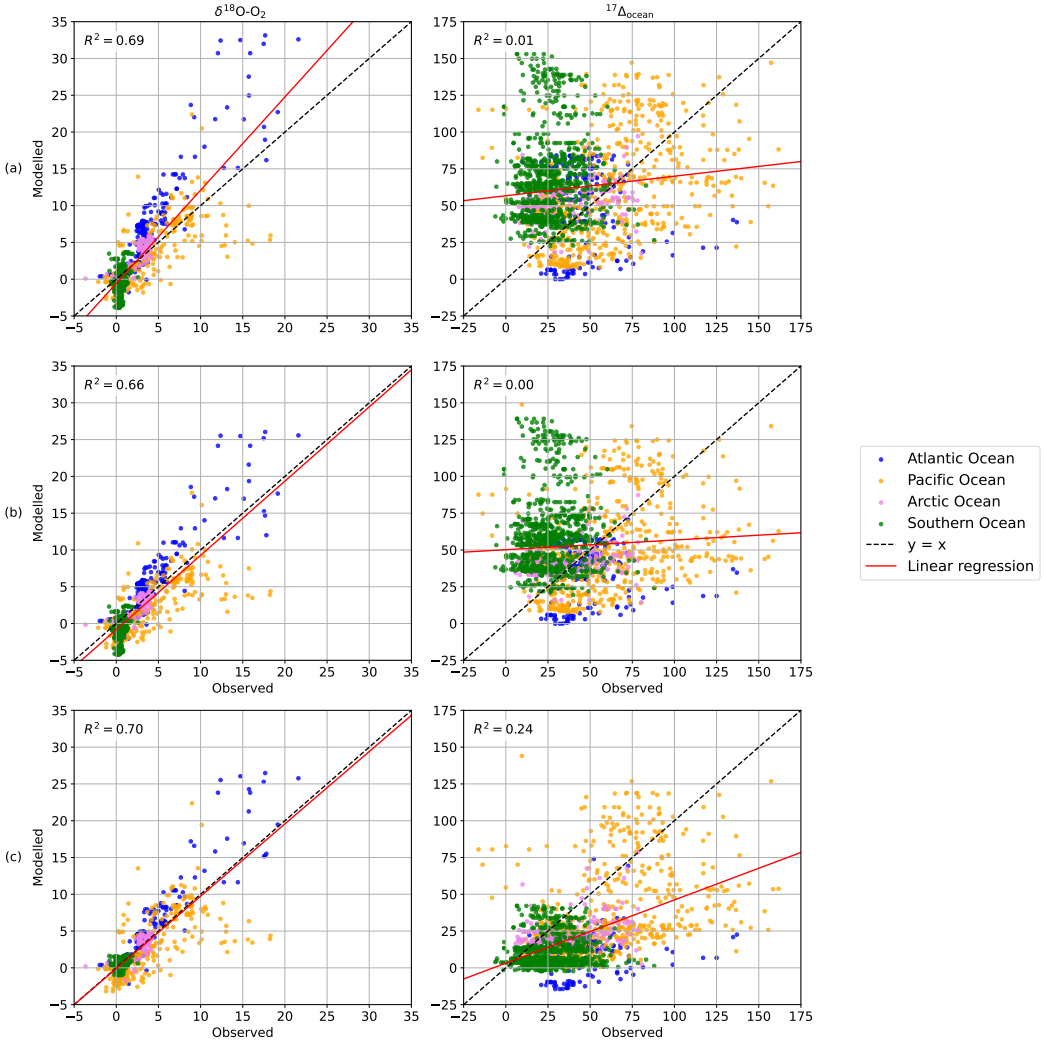

Figure 7. Linear regression applied between observed and modelled points for (a) the CTRL simulation, (b) the best combination for the global ocean, i.e. simulation 246 and (c) the simulation with 50% reduction in phytoplankton biomass in the Southern Ocean. The left column corresponds to the comparison for δ^{18}O–O$_2$, and the right column for $^{17}\Delta_{ocean}$. Each point in the model corresponds to the location of the measured point and takes seasonality into account.

For both tracers, the coefficients of determination (R^2) show no significant improvement in simulation 246 relative to CTRL. In contrast, the reduced-phytoplankton simulation yields improved coefficients of determination for both δ^{18}O–O$_2$ and $^{17}\Delta_{ocean}$, along with a reduced dispersion of these tracers in the Southern Ocean, confirming the influence of excessive photosynthetic activity in this region on model performance (Figure 7). Nevertheless, R^2 for $^{17}\Delta_{ocean}$ remain relatively low across all simulations, reflecting subgrid-scale variability that cannot be resolved by iLOVECLIM, which represents grid-cell averages rather than individual observations. Consequently, even optimized parametrizations fail to fully reproduce the observed $^{17}\Delta_{ocean}$ signal. Indeed, while basin-specific tuning of fractionation coefficients could potentially improve the representation of δ^{18}O–O$_2$, which is already reasonably well simulated, such refinements are unlikely to significantly enhance the representation of $^{17}\Delta_{ocean}$.

These tracers reflect the distribution of oxygen isotopes governed by key processes, including photosynthesis, respiration, and air-sea gas exchange. Across the Atlantic, Pacific, and Arctic Oceans, $\delta^{18}O–O_2$ is more accurately represented in terms of variability than $^{17}\Delta_{ocean}$ (Figure 6, Figure 7, Figure B1). This contrast reflects their sensitivities to biological processes: $\delta^{18}O–O_2$ integrates both photosynthetic and respiratory effects, which tend to partially compensate for each other, whereas $^{17}\Delta_{ocean}$ is primarily driven by photosynthesis and is therefore more sensitive to local variability and model biases (Figure 3). The comparatively good agreement for $\delta^{18}O–O_2$, contrasted with the remaining discrepancies in $^{17}\Delta_{ocean}$, suggests that some processes specifically affecting $^{17}\Delta_{ocean}$ may still be insufficiently represented or constrained. This mismatch is further exacerbated by unresolved subgrid-scale variability, which contributes to the persistent difference between modelled and observed $^{17}\Delta_{ocean}$. Although the iLOVECLIM model includes the major known processes, these discrepancies likely reflect limitations in the representation of phytoplankton distribution and associated photosynthetic fractionation, particularly in the Southern Ocean. In addition, the relatively sparse observational coverage limits the robustness of model–data comparisons. Altogether, these results highlight the strong sensitivity of $^{17}\Delta_{ocean}$ to photosynthetic activity and underscore the need for improved constraints on photosynthetic fractionation, expanded observational datasets, and further investigation into the fine-scale processes controlling $^{17}\Delta_{ocean}$ variability.

5 Conclusions

In this study, we examined $\delta^{18}O–O_2$ and $^{17}\Delta_{ocean}$ at different scales. These isotopic tracers are computed for the first time in a coupled Earth system model iLOVECLIM, based on the representation of oxygen isotopes. Consequently, both tracers depend on the same simulated $^{32}O_2$, $^{33}O_2$, and $^{34}O_2$, and are therefore influenced by the same processes implemented in our iLOVECLIM model.

At the largest scale, oxygen isotopic tracers exhibit spatial distributions structured by climatological and environmental variables. Based on a Spearman correlation and principal component analysis, three dominant groups were identified: hydrological, biological, and chemical. While $\delta^{18}O–O_2$ integrates contributions from all three groups, $^{17}\Delta_{ocean}$ appears to be more strongly influenced by residuals processes affecting dissolved oxygen.

At an intermediate scale, four main processes were investigated: photosynthesis, respiration, ocean-atmosphere exchange, and other unresolved physical processes such as ocean circulation. The deconvolution of isotopic signals highlights respiration as the primary control on $\delta^{18}O–O_2$, whereas photosynthesis emerges as the dominant control on $^{17}\Delta_{ocean}$. Moreover, photosynthetic and physical processes exert opposing influence on the isotopic proxies. While these results improve our mechanistic understanding of these proxies, they remain sensitive to the biological fractionation coefficients applied in the model.

At smaller scales, sensitivity experiments based on a Latin hypercube approach show that respiration-related fractionations are tightly constrained and are independent parameters, with $^{17/18}\theta_{resp}$ close to 0.517 and $^{18}\alpha_{resp}$ decreasing with depth. In contrast, photosynthetic fractionations can vary as long as the dependence between $^{18}\alpha_{photo}$ and $^{17/18}\theta_{photo}$ is respected, corresponding to a photosynthetic signal of 226 ppm. Simulation 246 emerges as the best compromise parametrization at the global scale, reproducing the main features of both $\delta^{18}O–O_2$ and $^{17}\Delta_{ocean}$. However, even when photosynthetic fractionations are optimized, the variability of $^{17}\Delta_{ocean}$ is not fully captured in the surface ocean. While the tracer is reasonably well reproduced in the deep ocean, its surface signal is dominated by fine-scale variability driven by local interactions between oceanographic conditions and biological productivity. This results in a highly heterogeneous surface distribution, which prevents the emergence of a robust large-scale signal. Although some features, such as the subsurface maximum and deep stabilization are captured, the

deep-ocean signal ultimately inherits surface biological activity and is therefore indirectly controlled by highly local processes, including seasonal mixed-layer dynamics, local productivity maxima and ocean circulation.

More broadly, these results highlight both observational and model limitations. The observational dataset remains sparse and unevenly distributed, with measurements reflecting local conditions at specific times, limiting the ability to constrain large-scale patterns. In the model, the overestimation of $^{17}\Delta_{\text{ocean}}$ in the Southern Ocean confirms its strong sensitivity to photosynthetic processes and also suggests a bias in the representation of phytoplankton in this area. However, the good agreement obtained for δ^{18}O–O_2 indicates that the major processes governing oxygen isotopes are realistically represented in iLOVECLIM. In contrast, the inability to fully reproduce $^{17}\Delta_{\text{ocean}}$ in the ocean surface suggests that additional processes, or poorly constrained mechanisms, may influence this tracer beyond those currently implemented. Further work is therefore needed to better characterize these processes and improve both model parameterizations and observational coverage in order to fully exploit $^{17}\Delta_{\text{ocean}}$ as a marine isotopic proxy.

Appendix A Cross section of the Atlantic and Pacific basins

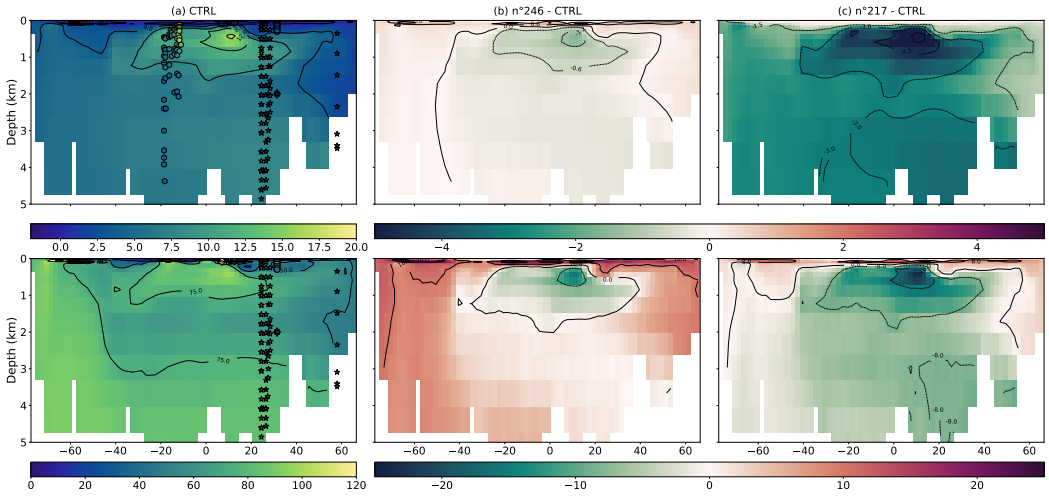

Figure A1. Cross-section of the Atlantic Ocean for the simulation (a) CTRL, (b) the best global simulation (246), (c) the best simulation for the Atlantic Ocean (217). In panel a, the points represent observed data. In panels b and c, the background represents the anomaly between the simulation and the CTRL reference simulation. The first line corresponds to δ^{18}O–O_2 and the second line to $^{17}\Delta_{\text{ocean}}$ results.

At the basin scale, the Atlantic Ocean provides a clear illustration of the impact of biological fractionation on the simulated isotopic proxies. The responses obtained with simulation 246 are compared with those of the simulation that performs best at the basin scale (217). In both simulations, respiration-related fractionation coefficients induce a decrease in δ^{18}O–O_2. In contrast, the combined effects of respiration and photosynthetic fractionation lead again to a more complex response of $^{17}\Delta_{\text{ocean}}$, reflecting the opposing influences of the two biological processes. Figure A1 illustrates the spatial patterns associated with these different fractionation coefficient combinations. For δ^{18}O–O_2, the applied fractionations lead to decreases of up to approximately -5 ppm in regions characterized by high respiration rates. For $^{17}\Delta_{\text{ocean}}$, fractionation effects induce decreases in high-respiration regions and in the deep ocean, reaching values of up to approximately

-15 ppm, whereas increases of about 15 ppm are observed within the photic layer, reflecting the influence of photosynthetic fractionation. Similar spatial responses are observed in the Pacific Ocean (Figure A2). For each basin, simulation 246 reproduces these general patterns, albeit with more moderate amplitudes, consistent with its role as a compromise parameterization designed to provide an adequate representation across multiple ocean basins.

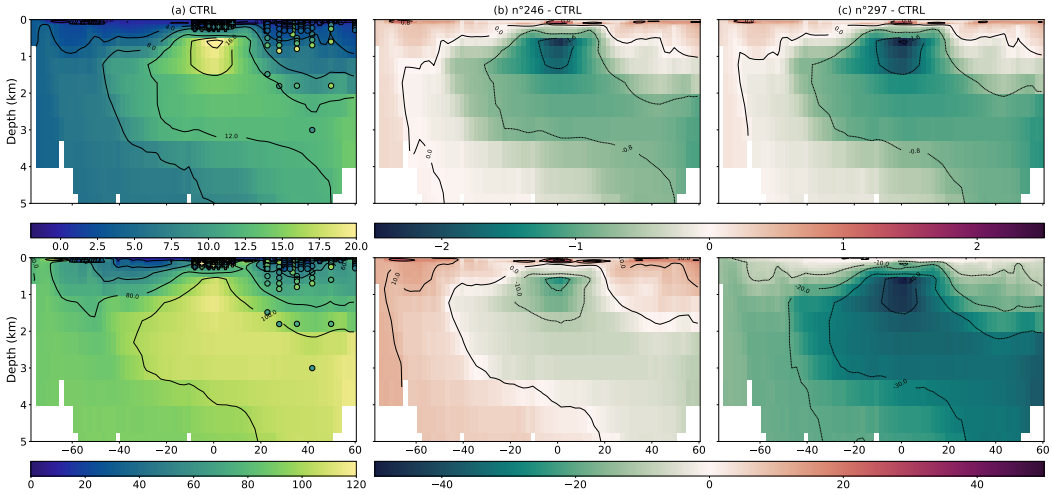

Figure A2. Cross-section of the Pacific Ocean for the simulation (a) CTRL, (b) the best global simulation (246), (c) the best simulation for the Pacific Ocean (297). In panel a, the points represent observed data. In panels b and c, the background represents the anomaly between the simulation and the CTRL reference simulation. The first line corresponds to $\delta^{18}O–O_2$ and the second line to $^{17}\Delta_{ocean}$ results.

Appendix B Arctic and Southern Oceans

Both $\delta^{18}O–O_2$ and $^{17}\Delta_{ocean}$ exhibit comparable ranges of variability across the major ocean basins (Figure 6; Figure B1). As in the Atlantic and Pacific Oceans, the simulated $\delta^{18}O–O_2$ and $^{17}\Delta_{ocean}$ signals in the Arctic Ocean are well reproduced in terms of both amplitude and spatial patterns (Figure B1). In contrast, the range of variability is not well reproduced in the Southern Ocean (Figure B2), particularly for the $^{17}\Delta_{ocean}$. Observed $^{17}\Delta_{ocean}$ varies range from 0 to 90 ppm, whereas the model simulates a broader and shift range of 10 to 150 ppm.

This discrepancy highlights the strong sensitivity of $^{17}\Delta_{ocean}$ of intense biological activity. Given that $\delta^{18}O–O_2$ remains generally within the observed range, this suggest that the mismatch is more specifically related to the representation of photosynthetic process, and possibly to biases in phytoplankton distribution in the Southern Ocean.

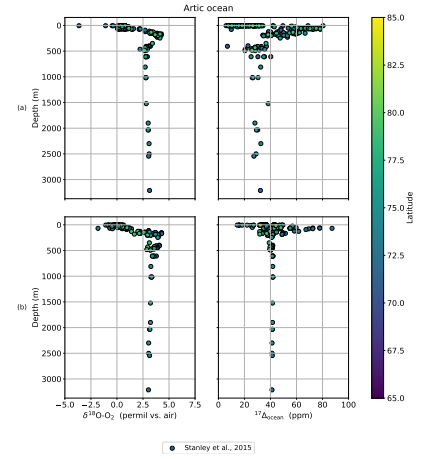

Figure B1. Analysis of $\delta^{18}O$–O_2 and $^{17}\Delta_{ocean}$ in Arctic Ocean, from (a) measured data versus (b) modelled data from the best combination for the global ocean, i.e. simulation 246. Each point in the model corresponds to the location of the measured point and takes seasonality into account.

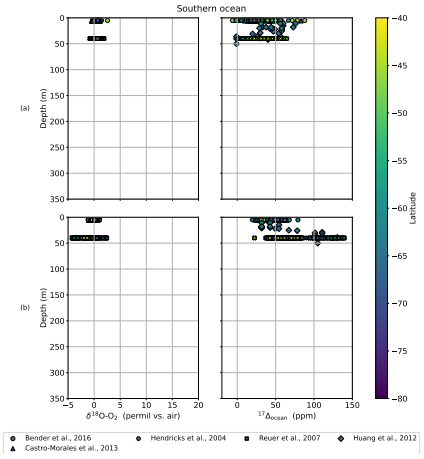

Figure B2. Analysis of $\delta^{18}O$–O_2 and $^{17}\Delta_{ocean}$ in Southern Ocean, from (a) measured data versus (b) modelled data from the best combination for the global ocean, i.e. simulation 246. Each point in the model corresponds to the location of the measured point and takes seasonality into account.

Open Research Section

The source code of the iLOVECLIM model used in this study (version 1.1.7) is archived on Zenodo (DOI: https://doi.org/10.5281/zenodo.17379487, Clermont and Roche (2025)). For further information about the code, please contact Didier M. Roche (didier.roche@lsce.ipsl.fr).

All model outputs used to generate the figures in this study are available on Zenodo (DOI: https://doi.org/10.5281/zenodo.19892438, Clermont (2026)). Observational datasets used for model–data comparison are either publicly available from the original cited sources or have been compiled and included in the Zenodo repository. All corresponding references for these datasets are provided in the Application section (3.3). The dataset described in Stanley et al. (2015) is publicly available at: http://www.whoi.edu/beaufortgyre.

$^{17}\Delta_{ocean}$ measurements from the BAT and HOT stations were taken from D. P. Nicholson et al. (2012). The dataset analyzed in M. L. Bender et al. (2016) and Li et al. (2022) come from Argo (2025) and Hu et al. (2018), respectively.

Conflict of Interest disclosure

The authors declare there are no conflicts of interest for this manuscript.

Acknowledgments

The authors thank Melissa Hendricks for sharing her dataset from the equatorial Pacific and Southern Oceans, and Aurélien Quiquet for providing the Latin Hypercube sampling method and associated script.

This research was funded, in whole or in part, by the Agence Nationale de la Recherche (ANR), grant ANR-22-CPJ1-0081-01, awarded to JWY. EC acknowledges support from the Ministère de l'Enseignement supérieur, de la Recherche et de l'Innovation.

References

Argo. (2025). *Argo float data and metadata from Global Data Assembly Centre (Argo GDAC).* SEANOE. Retrieved 2025-10-07, from https://www.seanoe.org/data/00311/42182/ doi: 10.17882/42182

Ash, J., Hu, H., & Yeung, L. (2020). What fractionates oxygen isotopes during respiration? Insights from multiple isotopologue measurements and theory. *ACS Earth and Space Chemistry*, *4*(1), 50–66. doi: https://doi.org/10.1021/acsearthspacechem.9b00230

Bender, M., Sowers, T., & Labeyrie, L. (1994, September). The Dole Effect and its variations during the last 130,000 years as measured in the Vostok Ice Core. *Global Biogeochemical Cycles*, *8*(3), 363–376. Retrieved 2025-09-09, from https://agupubs.onlinelibrary.wiley.com/doi/10.1029/94GB00724 doi: 10.1029/94GB00724

Bender, M. L. (1990, December). The \(\delta^{18}\)O of dissolved O\textsubscript{2} in seawater: A unique tracer of circulation and respiration in the deep sea. *J. Geophys. Res.*, *95*(C12), 22243–22252. Retrieved 2024-02-09, from https://agupubs.onlinelibrary.wiley.com/doi/10.1029/JC095iC12p22243 doi: 10.1029/JC095iC12p22243

Bender, M. L., & Grande, K. D. (1987). Production, respiration, and the isotope geochemistry of O2 in the upper water column. *Global Biogeochemical Cycles*, *1*(1), 49–59. Retrieved 2025-07-24, from https://onlinelibrary.wiley.com/doi/abs/10.1029/GB001i001p00049 (_eprint: https://agupubs.onlinelibrary.wiley.com/doi/pdf/10.1029/GB001i001p00049) doi: 10.1029/GB001i001p00049

Bender, M. L., Tilbrook, B., Cassar, N., Jonsson, B., Poisson, A., & Trull, T. W. (2016, June). Ocean productivity south of Australia during spring and summer. *Deep Sea Research Part I: Oceanographic Research Papers*, *112*, 68–78. Retrieved 2025-10-06, from https://www.sciencedirect.com/science/article/pii/S0967063715301862 doi: 10.1016/j.dsr.2016.02.018

Bienville, N., Landais, A., Fiorini, S., Piel, C., Sauze, J., Lemaire, B., ... Dapoigny, A. (2026, April). An intermediary scale setup to measure O_2 fractionation factors of aquatic biosphere. *EGUsphere*, 1–24. Retrieved 2026-04-17, from https://egusphere.copernicus.org/preprints/2026/egusphere-2026-1369/ doi: 10.5194/egusphere-2026-1369

Bouttes, N., Roche, D. M., Mariotti, V., & Bopp, L. (2015, May). Including an ocean carbon cycle model into *i*LOVECLIM (v1.0). *Geosci. Model Dev.*,

8(5), 1563–1576. Retrieved 2025-09-09, from https://gmd.copernicus.org/articles/8/1563/2015/ doi: 10.5194/gmd-8-1563-2015

Castro-Morales, K., Cassar, N., Shoosmith, D. R., & Kaiser, J. (2013, April). Biological production in the Bellingshausen Sea from oxygen-to-argon ratios and oxygen triple isotopes. *Biogeosciences*, *10*(4), 2273–2291. Retrieved 2025-10-06, from https://bg.copernicus.org/articles/10/2273/2013/ doi: 10.5194/bg-10-2273-2013

Clermont, E. (2026, April). *ILOVECLIM model outputs for ocean oxygen isotopes: PCA, process deconvolution, and model–data comparison.* Zenodo. Retrieved 2026-04-29, from https://zenodo.org/records/19892438 doi: 10.5281/zenodo.19892438

Clermont, E., & Roche, D. M. (2025, October). *iLOVECLIM source code (version 1.1.7).* Zenodo. Retrieved 2025-10-17, from https://zenodo.org/records/17379487 doi: 10.5281/zenodo.17379487

Clermont, E., Yang, J.-W., Roche, D. M., & Extier, T. (2026). Including the triple isotopic composition of dissolved oxygen in the ocean into the iLOVECLIM model (version 1.1.7): development and evaluation. *EGUsphere*, *2026*, 1–27. Retrieved from https://egusphere.copernicus.org/preprints/2026/egusphere-2025-5230/ doi: 10.5194/egusphere-2025-5230

Eisenstadt, D., Barkan, E., Luz, B., & Kaplan, A. (2010, February). Enrichment of oxygen heavy isotopes during photosynthesis in phytoplankton. *Photosynth Res*, *103*(2), 97–103. Retrieved 2026-02-11, from https://doi.org/10.1007/s11120-009-9518-z doi: 10.1007/s11120-009-9518-z

Friedlingstein, P., O'Sullivan, M., Jones, M. W., Andrew, R. M., Bakker, D. C. E., Hauck, J., ... Zeng, J. (2025, November). Global Carbon Budget 2025. *Earth System Science Data Discussions*, 1–139. Retrieved 2026-04-13, from https://essd.copernicus.org/preprints/essd-2025-659/ doi: 10.5194/essd-2025-659

Goosse, H., Brovkin, V., Fichefet, T., Haarsma, R., Huybrechts, P., Jongma, J., ... Weber, S. L. (2010, November). Description of the Earth system model of intermediate complexity LOVECLIM version 1.2. *Geosci. Model Dev.*, *3*(2), 603–633. Retrieved 2025-09-09, from https://gmd.copernicus.org/articles/3/603/2010/ doi: 10.5194/gmd-3-603-2010

Goosse, H., & Fichefet, T. (1999, October). Importance of ice-ocean interactions for the global ocean circulation: A model study. *J. Geophys. Res.*, *104*(C10), 23337–23355. Retrieved 2025-09-09, from https://agupubs.onlinelibrary.wiley.com/doi/10.1029/1999JC900215 doi: 10.1029/1999JC900215

Guy, R. D., Berry, J. A., Fogel, M. L., & Hoering, T. C. (1989, April). Differential fractionation of oxygen isotopes by cyanide-resistant and cyanide-sensitive respiration in plants. *Planta*, *177*(4), 483–491. Retrieved 2024-04-02, from http://link.springer.com/10.1007/BF00392616 doi: 10.1007/BF00392616

Helman, Y., Barkan, E., Eisenstadt, D., Luz, B., & Kaplan, A. (2005, August). Fractionation of the Three Stable Oxygen Isotopes by Oxygen-Producing and Oxygen-Consuming Reactions in Photosynthetic Organisms. *Plant Physiology*, *138*(4), 2292–2298. Retrieved 2025-09-09, from https://academic.oup.com/plphys/article/138/4/2292/6112998 doi: 10.1104/pp.105.063768

Hendricks, M. B., Bender, M. L., & Barnett, B. A. (2004, November). Net and gross O2 production in the southern ocean from measurements of biological O2 saturation and its triple isotope composition. *Deep Sea Research Part I: Oceanographic Research Papers*, *51*(11), 1541–1561. Retrieved 2025-09-09, from https://linkinghub.elsevier.com/retrieve/pii/S0967063704001153 doi: 10.1016/j.dsr.2004.06.006

Hendricks, M. B., Bender, M. L., Barnett, B. A., Strutton, P., & Chavez, F. P.

(2005, December). Triple oxygen isotope composition of dissolved O_2 in the equatorial Pacific: A tracer of mixing, production, and respiration. *J. Geophys. Res.*, *110*(C12), 2004JC002735. Retrieved 2025-09-09, from https://agupubs.onlinelibrary.wiley.com/doi/10.1029/2004JC002735 doi: 10.1029/2004JC002735

Hu, H., Yeung, L., Berelson, W., & Young, E. (2018). *Depth profiles of dissolved O2 saturation and isotopologues from the R/V Yellowfin and R/V Kilo Moana from 2016-09-14 to 2017-08-28.* Biological and Chemical Oceanography Data Management Office (BCO-DMO). doi: 10.1575/1912/bco-dmo.753594.1

Huang, K., Ducklow, H., Vernet, M., Cassar, N., & Bender, M. L. (2012). Export production and its regulating factors in the West Antarctica Peninsula region of the Southern Ocean. *Global Biogeochemical Cycles*, *26*. Retrieved 2025-10-06, from https://agupubs.onlinelibrary.wiley.com/doi/full/10.1029/2010GB004028 doi: 10.1029/2010GB004028.

Johnson, R. J., Bates, N., Lethaby, P. J., Smith, D., Medley, C., Stuart, E., & May, R. (2025, June). *Primary productivity estimates from the incubation of seawater collected at the Bermuda Atlantic Time-series Study (BATS) site from December 1988 through December 2024.* Biological and Chemical Oceanography Data Management Office (BCO-DMO). Retrieved 2025-10-07, from https://hdl.handle.net/1912/71903 doi: 10.26008/1912/BCO-DMO.893182.6

Juranek, L., & Quay, P. (2013, January). Using Triple Isotopes of Dissolved Oxygen to Evaluate Global Marine Productivity. *Annu. Rev. Mar. Sci.*, *5*(1), 503–524. Retrieved 2025-09-09, from https://www.annualreviews.org/doi/10.1146/annurev-marine-121211-172430 doi: 10.1146/annurev-marine-121211-172430

Juranek, L. W., & Quay, P. D. (2010, June). Basin-wide photosynthetic production rates in the subtropical and tropical Pacific Ocean determined from dissolved oxygen isotope ratio measurements. *Global Biogeochemical Cycles*, *24*(2), 2009GB003492. Retrieved 2025-09-09, from https://agupubs.onlinelibrary.wiley.com/doi/10.1029/2009GB003492 doi: 10.1029/2009GB003492

Juranek, L. W., Quay, P. D., Feely, R. A., Lockwood, D., Karl, D. M., & Church, M. J. (2012). Biological production in the NE Pacific and its influence on air-sea CO2 flux: Evidence from dissolved oxygen isotopes and O2/Ar. *Journal of Geophysical Research: Oceans*, *117*(C5). Retrieved 2025-10-06, from https://onlinelibrary.wiley.com/doi/abs/10.1029/2011JC007450 (_eprint: https://agupubs.onlinelibrary.wiley.com/doi/pdf/10.1029/2011JC007450) doi: 10.1029/2011JC007450

Kiddon, J., Bender, M. L., Orchardo, J., Caron, D. A., Goldman, J. C., & Dennett, M. (1993, September). Isotopic fractionation of oxygen by respiring marine organisms. *Global Biogeochemical Cycles*, *7*(3), 679–694. Retrieved 2025-09-09, from https://agupubs.onlinelibrary.wiley.com/doi/10.1029/93GB01444 doi: 10.1029/93GB01444

Kroopnick, P., & Craig, H. (1976). OXYGEN ISOTOPE FRACTIONATION IN DISSOLVED OXYGEN IN THE DEEP SEA.

Kroopnick, P. M. (1975). Respiration, photosynthesis, and oxygen isotope fractionation in oceanic surface water. *Limnology and Oceanography*, *20*(6), 988–992. Retrieved 2026-02-11, from https://onlinelibrary.wiley.com/doi/abs/10.4319/lo.1975.20.6.0988 (_eprint: https://aslopubs.onlinelibrary.wiley.com/doi/pdf/10.4319/lo.1975.20.6.0988) doi: 10.4319/lo.1975.20.6.0988

Levine, N. M., Bender, M. L., & Doney, S. C. (2009, March). The {\(\delta^{18}\)}O of dissolved O\textsubscript{2} as a tracer of mixing and respiration in the mesopelagic ocean. *Global Biogeochemical Cycles*, *23*(1),

2007GB003162. Retrieved 2025-09-09, from https://agupubs.onlinelibrary.wiley.com/doi/10.1029/2007GB003162 doi: 10.1029/2007GB003162

Li, B., Hu, H., Berelson, W. M., Adkins, J. F., & Yeung, L. Y. (2022, December). On the Use of Dissolved Oxygen Isotopologues as Biogeochemical Tracers in the Northeast Pacific Ocean. *JGR Oceans*, *127*(12), e2022JC018617. Retrieved 2025-09-09, from https://agupubs.onlinelibrary.wiley.com/doi/10.1029/2022JC018617 doi: 10.1029/2022JC018617

Luz, B., & Barkan, E. (2000, June). Assessment of Oceanic Productivity with the Triple-Isotope Composition of Dissolved Oxygen. *Science*, *288*(5473), 2028–2031. Retrieved 2025-09-09, from https://www.science.org/doi/10.1126/science.288.5473.2028 doi: 10.1126/science.288.5473.2028

Luz, B., & Barkan, E. (2005, March). The isotopic ratios 17O/16O and 18O/16O in molecular oxygen and their significance in biogeochemistry. *Geochimica et Cosmochimica Acta*, *69*(5), 1099–1110. Retrieved 2025-09-09, from https://linkinghub.elsevier.com/retrieve/pii/S001670370400660X doi: 10.1016/j.gca.2004.09.001

Luz, B., & Barkan, E. (2009). Net and gross oxygen production from O2/Ar, 17O/16O and 18O/16O ratios. *Aquatic Microbial Ecology*, *56*(2-3), 133–145. doi: 10.3354/ame01296

Luz, B., & Barkan, E. (2011a). The isotopic composition of atmospheric oxygen. *Global Biogeochemical Cycles*, *25*(3). Retrieved 2026-02-11, from https://onlinelibrary.wiley.com/doi/abs/10.1029/2010GB003883 (_eprint: https://agupubs.onlinelibrary.wiley.com/doi/pdf/10.1029/2010GB003883) doi: 10.1029/2010GB003883

Luz, B., & Barkan, E. (2011b). Proper estimation of marine gross O\textsubscript{2} production with 17O/16O and 18O/16O ratios of dissolved O\textsubscript{2}. *Geophysical Research Letters*, *38*(19). Retrieved 2026-02-11, from https://onlinelibrary.wiley.com/doi/abs/10.1029/2011GL049138 (_eprint: https://agupubs.onlinelibrary.wiley.com/doi/pdf/10.1029/2011GL049138) doi: 10.1029/2011GL049138

Luz, B., Barkan, E., Bender, M. L., Thiemens, M. H., & Boering, K. A. (1999, August). Triple-isotope composition of atmospheric oxygen as a tracer of biosphere productivity. *Nature*, *400*(6744), 547–550. Retrieved 2025-09-09, from https://www.nature.com/articles/22987 doi: 10.1038/22987

Luz, B., Barkan, E., Sagi, Y., & Yacobi, Y. Z. (2002, January). Evaluation of community respiratory mechanisms with oxygen isotopes: A case study in Lake Kinneret. *Limnology & Oceanography*, *47*(1), 33–42. Retrieved 2024-06-05, from https://aslopubs.onlinelibrary.wiley.com/doi/10.4319/lo.2002.47.1.0033 doi: 10.4319/lo.2002.47.1.0033

Miller, M. F. (2002). Isotopic fractionation and the quantification of 17O anomalies in the oxygen three-isotope system: an appraisal and geochemical significance.

Munro, D. R., Quay, P. D., Juranek, L. W., & Goericke, R. (2013, July). Biological production rates off the Southern California coast estimated from triple O_2 isotopes and O_2 : Ar gas ratios. *Limnology & Oceanography*, *58*(4), 1312–1328. Retrieved 2025-09-09, from https://aslopubs.onlinelibrary.wiley.com/doi/10.4319/lo.2013.58.4.1312 doi: 10.4319/lo.2013.58.4.1312

Musan, I., Gildor, H., Barkan, E., Smethie, W. M., & Luz, B. (2023, February). Evidence From Dissolved O_2 Isotopes in North Atlantic Deep Water for a Recent Climatic Shift. *Geophysical Research Letters*, *50*(3), e2022GL100489. Retrieved 2025-09-09, from https://agupubs.onlinelibrary.wiley.com/doi/10.1029/2022GL100489 doi: 10.1029/2022GL100489

Nicholson, D., Stanley, R. H. R., & Doney, S. C. (2014, May). The triple oxygen isotope tracer of primary productivity in a dynamic ocean model. *Global Biogeochemical Cycles*, *28*(5), 538–552. Retrieved 2025-09-09, from

https://agupubs.onlinelibrary.wiley.com/doi/10.1002/2013GB004704 doi: 10.1002/2013GB004704

Nicholson, D. P., Stanley, R. H. R., Barkan, E., Karl, D. M., Luz, B., Quay, P. D., & Doney, S. C. (2012, May). Evaluating triple oxygen isotope estimates of gross primary production at the Hawaii Ocean Time-series and Bermuda Atlantic Time-series Study sites. *J. Geophys. Res.*, *117*(C5), 2010JC006856. Retrieved 2025-09-09, from https://agupubs.onlinelibrary.wiley.com/doi/10.1029/2010JC006856 doi: 10.1029/2010JC006856

Opsteegh, J. D., Haarsma, R. J., Selten, F. M., & Kattenberg, A. (1998, January). ECBILT: a dynamic alternative to mixed boundary conditions in ocean models. *Tellus A: Dynamic Meteorology and Oceanography*, *50*(3), 348. Retrieved 2025-09-09, from https://a.tellusjournals.se/article/10.3402/tellusa.v50i3.14524/ doi: 10.3402/tellusa.v50i3.14524

Palevsky, H. I., Quay, P. D., Lockwood, D. E., & Nicholson, D. P. (2016, February). The annual cycle of gross primary production, net community production, and export efficiency across the North Pacific Ocean. *Global Biogeochemical Cycles*, *30*(2), 361–380. Retrieved 2025-09-09, from https://agupubs.onlinelibrary.wiley.com/doi/10.1002/2015GB005318 doi: 10.1002/2015GB005318

Quay, P. D., Emerson, S., Wilbur, D. O., Stump, C., & Knox, M. (1993). The δ^{18}O of dissolved O$_2$ in the surface waters of the subarctic Pacific: A tracer of biological productivity. *Journal of Geophysical Research: Oceans*, *98*(C5), 8447–8458. Retrieved 2024-02-09, from https://onlinelibrary.wiley.com/doi/abs/10.1029/92JC03017 (_eprint: https://onlinelibrary.wiley.com/doi/pdf/10.1029/92JC03017) doi: 10.1029/92JC03017

Quay, P. D., Wilbur, D. ., Richey, J. E., Devol, A. H., Benner, R., & Forsberg, B. R. (1995, June). The 18O:16O of dissolved oxygen in rivers and lakes in the Amazon Basin: Determining the ratio of respiration to photosynthesis rates in freshwaters. *Limnol. Oceanogr.*, *40*(4), 718–729. Retrieved 2025-09-09, from http://doi.wiley.com/10.4319/lo.1995.40.4.0718 doi: 10.4319/lo.1995.40.4.0718

Reuer, M. K., Barnett, B. A., Bender, M. L., Falkowski, P. G., & Hendricks, M. B. (2007, June). New estimates of Southern Ocean biological production rates from O2/Ar ratios and the triple isotope composition of O2. *Deep Sea Research Part I: Oceanographic Research Papers*, *54*(6), 951–974. Retrieved 2025-09-09, from https://linkinghub.elsevier.com/retrieve/pii/S0967063707000489 doi: 10.1016/j.dsr.2007.02.007

Roche, D. M., Dokken, T. M., Goosse, H., Renssen, H., & Weber, S. L. (2007). Climate of the Last Glacial Maximum: sensitivity studies and model-data comparison with the LOVECLIM coupled model. *Clim. Past*, *3*(2), 205–224. Retrieved from https://cp.copernicus.org/articles/3/205/2007/ doi: https://doi.org/10.5194/cp-3-205-2007

Sarma, V. V. S. S., Abe, O., & Saino, T. (2008). Spatial variations in time-integrated plankton metabolic rates in Sagami Bay using triple oxygen isotopes and O2:Ar ratios. *Limnology and Oceanography*, *53*(5), 1776–1783. Retrieved 2025-10-06, from https://onlinelibrary.wiley.com/doi/abs/10.4319/lo.2008.53.5.1776 (_eprint: https://aslopubs.onlinelibrary.wiley.com/doi/pdf/10.4319/lo.2008.53.5.1776) doi: 10.4319/lo.2008.53.5.1776

Schleser, G. H. (1979, March). Oxygen isotope fractionation during respiration for different temperatures ofT. utilis andE. coli K12. *Radiat Environ Biophys*, *17*(1), 85–93. Retrieved 2025-12-08, from https://doi.org/10.1007/BF01323122 doi: 10.1007/BF01323122

Stanley, R. H. R., Sandwith, Z. O., & Williams, W. J. (2015, July). Rates of

summertime biological productivity in the Beaufort Gyre: A comparison between the low and record-low ice conditions of August 2011 and 2012. *Journal of Marine Systems*, *147*, 29–44. Retrieved 2025-10-06, from https://www.sciencedirect.com/science/article/pii/S0924796314000839 doi: 10.1016/j.jmarsys.2014.04.006

Stevens, C. L. R., Schultz, D., Van Baalen, C., & Parker, P. L. (1975, July). Oxygen Isotope Fractionation during Photosynthesis in a Blue-Green and a Green Alga 1 2. *Plant Physiol*, *56*(1), 126–129. Retrieved 2026-02-11, from https://doi.org/10.1104/pp.56.1.126 doi: 10.1104/pp.56.1.126

Stolper, D. A., Fischer, W. W., & Bender, M. L. (2018, November). Effects of temperature and carbon source on the isotopic fractionations associated with O2 respiration for 17O/16O and 18O/16O ratios in E. coli. *Geochimica et Cosmochimica Acta*, *240*, 152–172. Retrieved 2025-09-09, from https://linkinghub.elsevier.com/retrieve/pii/S0016703718304253 doi: 10.1016/j.gca.2018.07.039

Sutherland, K. M., Johnston, D. T., Hemingway, J. D., Wankel, S. D., & Ward, C. P. (2022, November). Revised microbial and photochemical triple-oxygen isotope effects improve marine gross oxygen production estimates. *PNAS Nexus*, *1*(5), pgac233. Retrieved 2025-09-09, from https://academic.oup.com/pnasnexus/article/doi/10.1093/pnasnexus/pgac233/6759432 doi: 10.1093/pnasnexus/pgac233

Thiemens, M. H., Jackson, T., Mauersberger, K., Schueler, B., & Morton, J. (1991). Oxygen isotope fractionation in stratospheric CO2. *Geophysical Research Letters*, *18*(4), 669–672. Retrieved 2025-09-09, from https://onlinelibrary.wiley.com/doi/abs/10.1029/91GL00121 (_eprint: https://agupubs.onlinelibrary.wiley.com/doi/pdf/10.1029/91GL00121) doi: 10.1029/91GL00121

Wurgaft, E., Musan, I., Rivlin, T., & Luz, B. (2022, August). Weak isotopic fractionation of dissolved O2 during community respiration. *Limnology & Oceanography*, *67*(8), 1794–1804. Retrieved 2025-09-09, from https://aslopubs.onlinelibrary.wiley.com/doi/10.1002/lno.12167 doi: 10.1002/lno.12167

Yeung, L. Y., Berelson, W. M., Young, E. D., Prokopenko, M. G., Rollins, N., Coles, V. J., ... Yager, P. L. (2012). Impact of diatom-diazotroph associations on carbon export in the Amazon River plume. *Geophysical Research Letters*, *39*(18). Retrieved 2025-09-24, from https://onlinelibrary.wiley.com/doi/abs/10.1029/2012GL053356 (_eprint: https://agupubs.onlinelibrary.wiley.com/doi/pdf/10.1029/2012GL053356) doi: 10.1029/2012GL053356